THESIS FOR THE DEGREE OF LICENTIATE OF ENGINEERING

Numerical Prediction of Propeller Induced Hull Pressure Pulses

MUYE GE

Department of Mechanics and Maritime Sciences
CHALMERS UNIVERSITY OF TECHNOLOGY
Göteborg, Sweden 2019

Numerical Prediction of Propeller Induced Pressure Pulses

MUYE GE

© MUYE GE, 2019

Report no 2019:12

Department of Mechanics and Maritime Sciences
Chalmers University of Technology
SE-412 96 Göteborg
Sweden
Telephone + 46 (0)31-772 1000

Printed by Chalmers Reproservice
Göteborg, Sweden 2019

Numerical Prediction of Propeller Induced Hull Pressure Pulses

MUYE GE
Department of Mechanics and Maritime Sciences
Chalmers University of Technology

Abstract

Ship propeller induced pressure pulses is one of the major sources of both onboard noise and vibration as well as underwater radiated noise. The need for accurate pressure pulse prediction is increasing due to rising concerns of environmental impacts and comfort and welfare of passengers and crews. More accurate pressure pulse prediction is needed to be able to reduce the margin between high efficiency propeller design and low pressure pulse propeller design.

Experimental approaches are used for pressure pulse assessments in the final verification stage where models are produced, but they are limited in early design work. Potential flow based methods have been used for early estimation of pressure pulses, but due to the complexity of the pressure pulse generation mechanisms, including interaction between hull and propeller and various types of cavitation, viscous numerical methods are being developing as a complement to potential flow method and a faster and cheaper alternative of experimental testing. This thesis deals with the numerical prediction of marine propeller induced pressure pulses adapted from typical experimental procedures, including both model scale and full scale marine propellers operating in open-water conditions and behind hull conditions with non-cavitating and cavitating flows. Simulations were conducted using open-source package OpenFOAM and commercial package Star-CCM+ with Reynolds-Averaged Navier-Stokes (RANS) method.

Studied cases show that for propellers in behind conditions, the present RANS approach can provide good accuracy regarding 1^{st} and 2^{nd} order BPF (Blade Passing Frequency) hull pressure pulses early in design stage. Higher order BPF pressure pulses were also predicted reasonably well, and different mechanisms inducing higher order BPF pressure pulses, including small tip clearance, transient cavitation appearance and sheet cavitation closure and its interaction with tip vortex cavitation, are outlined in the thesis. For model scale propellers operating under nearly uniform inflows, sheet cavitation is often over-predicted and an improved cavitation mass transfer model is proposed which take laminar separation as an additional inception criteria. Studies regarding mesh resolutions and scaling effects are also included in certain cases.

Keywords: Pressure pulses, RANS, OpenFOAM, Star-CCM+, cavitation

Acknowledgement

First of all, I would like to express my gratitude to my supervisor and examiner Professor Rickard E. Bensow for his guidance and patience. I was granted a large extent of freedom regarding research while when I am lost he always shows up there and pointing out the right directions. I am also very grateful to my co-supervisor Dr. Urban Svennberg, for his continuous support, encouragement and valuable experiences shared.

In addition, I would like to thank Dr. Marko Vikström and Rikard Johansson for opening the door of research. Colleagues together at division of Marine Technology provide a wonderful working environment. I would also like to express my gratitude to Johan Lundberg and Göran Grunditz for their support and encouragement throughout the project.

The research project is funded by Kongsberg Maritime through Kongsberg University Research Centre at Chalmers University of Technology. Simulations were performed on resources at Chalmers Centre for Computational Science and Engineering (C3SE) provided by the Swedish National Infrastructure for Computing (SNIC).

List of appended publications

Two papers are appended in the present thesis:

- **Paper I** M. Ge, U. Svennberg, and R. E. Bensow. "Numerical Investigation of Pressure Pulse Predictions for Propellers Mounted on an Inclined Shaft." *Proceedings of the Sixth International Symposium on Marine Propulsors*. Rome, Italy, 2019
- **Paper II** M. Ge, U. Svennberg, and R. E. Bensow. "Investigation on RANS Prediction of Propeller Induced Pressure Pulses and Sheet-tip Cavitation Interactions in Behind Hull Condition." *To be submitted*.

CONTENTS

LIST OF FIGURES

LIST OF TABLES

1

Introduction

1.1 Background

Shipping is the most economical way of freight transportation and contributes to the majority of world trade of cargo. As a major approach of ship propulsion, marine propellers are widely used and propeller design with high propulsion efficiency is the major quest for propeller designers. However, there are several side-effects generating design constraints including induced hull pressure pulses and radiated noise which have been getting more attention in recent years.

The noise level in the ocean has increased about 3 dB every decade in the period from 1950 to 2000 as reported in [1] as deduced from measurements recorded in a measurement point in the Northeast Pacific Ocean. This number is equivalent to the noise intensity level being doubled every ten years. According to more recent statistics [2], the trend is not slowing down as the global ship density increased about three times from 1990 to 2012. The impacts of ship radiated noise for the environment and sea creatures are drawing more attention as well. In [3] it has been found that the overlap between low frequency noise radiated by marine vessels and whale communication signals leads to a series of health hazard for these sea mammals, and especially the noise in low frequencies ranging from several propeller blade passing frequencies could travel as far as hundreds of kilometers. The arctic transportation path is a new hot spot. The existence of ice cover may change the propagation properties of generated noise and the impacts to arctic environments can be another constraint.

High levels of on-board vibration and noise also impose health hazards to the seafarers who are long-term exposed, including change of hearing sensitivity, resonance in air containing organs, disorientation and acoustic annoyance [4]. Regulations like IMO Resolution MSC.337 addresses limits of on board noise levels at different on-board areas according to exposure hours. The arising market of cruise vessel and yacht also require noise and vibration levels below certain

levels to maintain the comfort of passengers as the pressure fluctuation on the hull body above propellers is one of the major sources of hull vibrations. The prediction of under-water radiated noise usually relies on acoustic analogies which are highly dependent on near-field pressure fluctuation predictions, and studies show the high similarity between the two [5].

There are several major mechanisms influencing propeller induced pressure pulses. As a propulsion unit, the propulsion force is generated by pressure difference on the opposite blade sides when the curved blades are rotating. The spatial variation of blade position generate pressure variations and pressure waves to the surrounding medium. Besides, the local pressure close to the propeller blades might drop below saturation pressure where phase transfer from water to vapor would occur, referred to as cavitation. The cavitation types for marine propellers are classified according to the shape of different vapor structure, and the most common ones are shown in figure 1.1: sheet cavitation, tip vortex cavitation and bubble cavitation.

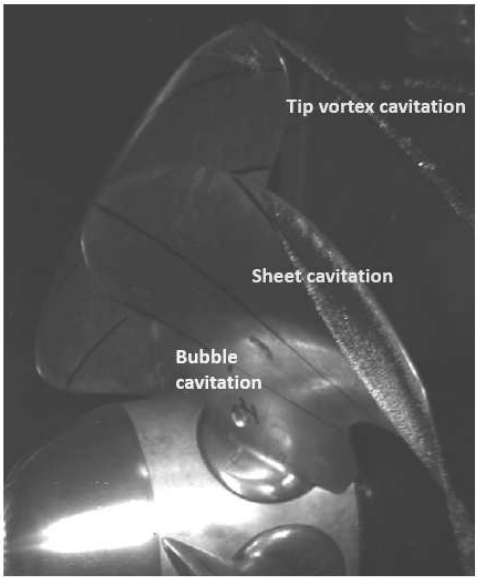

Figure 1.1: Common types of cavitation on a marine propeller

Experimental measurements are commonly used for propeller generated pressure pulses studies. Several approaches have been developed to determine the pressure pulse levels according to different types of configurations. Full scale ship measurement could provide the most reliable values but it is usually difficult to exclude the influences from sea states and due to the low transparency of sea water and limitation of view angles the cavitation patterns can usually not be seen clearly which could be vital for studies regarding pressure pulse generation. Besides, it is usually desired to predict the pressure pulse levels before the real ship is build. Experiments similar to Propeller Open-water Test (POT) could be conducted inside the cavitation tunnel and in order to create load variation to mimic

the working condition inside the ship wake, the propeller shaft is usually inclined or meshes and plates could be applied upstream of the propeller. Furthermore, the model scale ship hull could also be included in the cavitation tunnel, thus the propeller would be operating in an actual model scale ship wake. An even more challenging approach is to run the model scale ship with the propeller operating in a towing tank which needs to be depressurized. In the cavitation tunnel, a higher Reynolds number can usually be achieved which leads to a wake closer to full scale ship and with less risk of laminar-transition flow. For the configuration in a towing tank, usually Froude number similarity and cavitation number similarity must be maintained while a major concern is that the flow Reynolds number is usually even smaller than in a cavitation tunnel which might require special treatments.

Cavitation, if present, is one of the major sources of induced pressure pulses, however steady cavity structures are usually harmless regarding pressure pulses including sheet cavitation and tip vortex cavitation [6]. Due to the fact that marine propellers are usually working in the ship wake, the propeller-hull interaction plays an important role. The load on the propeller blade keeps changing while changing position inside the wake and usually increases at the wake peak and the induced pressure pulse would also increase locally. The cavitation structures are also varying while the blade is rotating in the ship wake and might contribute significantly regarding pressure pulse generation. The propeller induced pressure pulses are quite in phase with blade rotation, thus the pressure pulse levels are commonly shown in orders of blade passing frequency (BPF), and fast Fourier transformation (FFT) is widely used to analyse pressure pulse signals in the frequency domain.

It is believed that the 1^{st} and 2^{nd} order BPF fluctuations are caused by blade thickness and load for non-cavitating conditions and growth/shrinkage of propeller sheet cavitation for cavitating conditions. 3^{rd} and higher order BPF pressure pulses are believed to be originating from tip vortex cavitation related phenomenon while the knowledge is still building on. In [7], a series of high skew propeller models were studied experimentally in behind conditions and it was found that the tip vortex cavitation contributes to pressure pulses ranging in between 3^{rd} to 12^{th} orders BPF. In [8], the model scale propeller E779A was studied experimentally under non-uniform inflow and one of the deductions was that tip vortex cavitation contributes mainly to the 3^{rd} order BPF pressure pulse while the leading edge cavity contributes to the 4^{th} order BPF pressure pulse. More recently, in [9], the tip vortex cavitation was found to increase pressure pulse levels in the frequency range 400 hz to 2000 hz, which is approximately equivalent to 3^{rd} to 13^{th} orders BPF, and sheet cavitation, including its collapse and rebound, mainly contributes to blade frequency as well as higher order BPF pressure pulses. The tip vortex cavitation related phenomena were also found to be the source of a broadband hump in the amplitude spectrum [9] and the other known contribution to the hump is the cavitation differences between revolutions, which also reduces the tonal at higher harmonics of BPFs according to experimental studies in [10].

The ‘singing vortex’, termed in [11], was observed in experiments regarding cavitating foils which could cause significant increase of noise level and in [12] it is deduced that strong excitation is a must for such phenomena. Furthermore, the analytical model by Bosschers [13] and later studies [6] indicate that the active pulsing source comes from tip vortex cavitation inside the wake. In [14], the tip vortex bursting was found to be substantial in generating hull pressure pulses and later, in [15], the tip vortex bursting was experimentally found to be significantly influenced by the wake which the propellers were operating in and this phenomenon is referred to as sheet cavity closure in the studies in [16] where developed conceptual models of cavitation mechanisms regarding erosion including interaction between sheet cavity and tip vortex cavitation. Besides, in [17], various possible mechanisms were discussed regarding tip vortex cavitation induced pressure pulses. The tip clearance between the propeller blade tip and hull is another parameter that could be dominating in certain cases, as studied in [18]. The interaction between tip vortex cavitation and the rudder could also be pronounced as the tip vortex cavitation could become trapped in the gap between rudder and hull and collapse thus inducing significant levels of pressure pulses, as noticed in [19].

Numerical predictions of pressure pulses can be classified with increasing computational cost as by empirical approach, potential flow based approach and viscous flow based approach. For the potential flow based approach, Boundary Element Method (BEM), lifting line method, lifting surface method and other techniques can be found widely used. For the viscous flow based approach, RANS (Reynolds-Averaged Navier-Stokes) and LES (Large Eddy Simulation) as well as the combination between the two, DES (Detached Eddy Simulation) could be commonly found. The potential flow based approach and viscous flow based approach could be used separately or together to balance computational cost and accuracy. The empirical approach could also be used togehter with other approaches and the blended approaches are referred to as semi-empirical approaches. Besides, data driven models are also emerging [20].

RANS has been long used for marine applications including POT, resistance test, wake prediction as well as self-propulsion test and many research studies can be found using a RANS approach for pressure pulse predictions, including [21, 22] for numerical pressure pulse predictions with similar configurations according to POT and self-propulsion test. However, it is commonly regarded that the RANS approach can only accurately predict pressure pulses up to 2^{nd} BPF due to the diffculties in tip vortex prediction. Scale resolved turbulence models are used [23, 24, 25] for improved tip vortex predictions and in [26] numerical predictions using DDES were compared to full scale and model scale measurements. LES and DNS are still too expensive for this kind of predictions. In [27], the under-water noise generated by an operating propeller in behind condition using wall-modelled Implicit LES was assessed and suggested that hundreds of million cells would be needed to achieve anticipated resolution requirements. However, it is still a promising method, as in [28] also the internal jets are predicted which

could be another significant mechanism for pressure pulse formation. In [29], more than one hundred million cells were used for tip vortex cavitation inception predictions in POT-like conditions using ILES. In [30], the ILES was compared with RANS regarding tip vortex predictions for a stationary foil and in [31], DNS was applied in limited tip vortex zone and compared with RANS regarding tip vortex predictions. In both studies RANS predicted generally a more diffusive tip vortex but within limited distance downstream the foil, say around 5% $\sim$ 10% chord length, the minimum pressure agreed well with experimental measurements.

From the acoustics point of view, acoustic sources can be classified into three common types according to major modes of noise generation mechanisms: monopole, dipole and quadrupole sources. Regarding marine propellers, the dipole sources can be related with thickness noise (displacement of water medium) and load noise (forces on propeller blades) while the quadrupole sources are typically related with flow turbulence. Monopole source generates pressure waves with density change due to changes in volume thus related to cavitation. As demonstrated in figure 1.2, a breathing sphere with radius a and periodic surface velocity $v_A e^{i(\omega t - ka)}$ would generate onmi-directional pressure waves to the surrounding medium with density ρ_0 , and together with the wave equation and the linearized Bernoulli equation and neglecting density variation induced by acoustic waves, the pressure at a location outside the sphere at a time $p_{(r,t)}$could be derived as

$$p_{(r,t)} = \frac{1}{r}\frac{\rho_0 \omega a^2 v_A}{\sqrt{1+(ka)^2}} e^{i(\omega t - kr + arctan\frac{1}{ka})}. \tag{1.1}$$

By introducing conditions $r >> a$ and $a << \lambda$, the breathing sphere can be regarded as a point source and induced pressure fluctuation can be re-formulated as the time derivative of volume flow rate Q_A and second order derivative of total volume V_b regarding time, as shown in Equation 1.2.

$$p_{(r,t)} = i\omega \frac{\rho_0}{4\pi r} Q_A e^{i\omega(t-r/c_0)} = \frac{\rho_0}{4\pi r}\frac{\partial Q_A(t-r/c_0)}{\partial t} = \frac{\rho_0}{4\pi r}\frac{\partial^2 V_b(t-r/c_0)}{\partial t^2}. \tag{1.2}$$

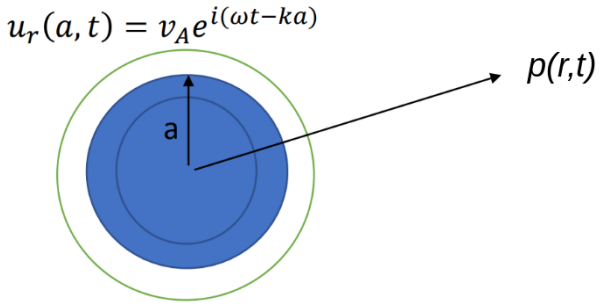

Figure 1.2: Pressure field induced by a breathing sphere source

The similarity between second order derivative of sheet cavitation volume and induced pressure pulses has been observed both experimentally and numerically [32, 33] while especially in [33] the cavity volume was put equal to a moving breathing sphere and estimated hull pressure pulses using the method of [34]. The estimated value agreed well with hull pressure pulses measured by pressure transducer. In [7] it was found that the volume of pulsing tip vortex cavitation could be related to the pressure pulse incidents in the time series recorded by hydrophones and according to [13] and [6], the tip vortex cavitation generate pressure pulses in a monopole manner when there are noticeably increasing noise levels.

1.2 Related terminology

The performance of a marine propeller is usually defined via non-dimensional propulsion coefficients, i.e. advance ratio J, thrust coefficient K_T, torque coefficient K_Q and open water efficiency η_o. These coefficients are defined as shown in Equation 1.3, in which V_A represents inlet flow velocity, n represents propeller rotation speed in rps, D represents propeller diameter, T represents propeller thrust, ρ represents fluid density and Q represents propeller torque,

$$J = \frac{V_A}{nD}, \quad K_T = \frac{T}{\rho n^2 D^4}, \quad K_Q = \frac{Q}{\rho_l n^2 D^5}, \quad \eta_o = \frac{JK_T}{2\pi K_Q}. \tag{1.3}$$

To achieve cavitation similarity in model scale experiments, the cavitation number should be equal to the full scale operating condition cavitation number. In the present thesis the cavitation number σ is defined as Equation 1.4 for behind conditions and as Equation 1.5 for open water conditions, which are based on the pressure difference with saturation pressure p_v with different reference values,

$$\sigma = \frac{p - p_v}{0.5\rho_l(\pi nD)^2}, \tag{1.4}$$

$$\sigma = \frac{p - p_v}{0.5\rho_l V_A^2}. \tag{1.5}$$

Pressure fluctuation $\hat{p}$ in model scale needs to be transformed to full scale, and the scaling is based on the non-dimensional coefficient K_p, which is assumed to be constant for model scale and full scale values. K_p is defined as,

$$K_p = \frac{\hat{p}}{\rho_l n^2 D^2}. \tag{1.6}$$

The chord length at 0.75 blade radius c_b are commonly used for blade Reynolds number calculation when studying marine propellers,

$$Re_b = \frac{c_b}{\nu}\sqrt{V_A^2 + (0.75\pi nD)^2}. \tag{1.7}$$

1.3 Research objectives

The research is focused on giving the scientific foundation for an engineering tool for prediction of pressure pulses subjected to the ship hull above the propeller. As pressure pulse induced noise and hull vibration are often required in contract to be below a certain level, more accurate pressure pulse prediction would make it possible to reduce the margin between high performance design and low pressure pulse design.

Numerical simulation with RANS approach is a preferred engineering tool which could provide more accurate predictions compared to BEM and less expensive than LES, thus selected to be the major simulation approach used in the present study. The first objective is to investigate the capability and limitations of the methodology in predicting hull pressure pulses aiming at 1^{st} and 2^{nd} blade passing frequencies regarding the commonly used experimental configurations.

Ideally the non-dimensional coefficients in Section 1.2 are identical comparing full-scale values and model-scale value. However, differences do exist which are referred to as scale effects. Typically it is believed for a model scale propeller with blade Reynolds number higher than 5×10^5 - 1×10^6, the scale effect is small regarding the force related propulsion coefficients but avoidance of laminar-transition surface flow requires much higher Reynolds number [35]. The assumption of similarity through equality of model scale cavitation number and full scale cavitation number $\sigma_m = \sigma_f$ does not always hold true, especially for cavitation inception. The cavitation phenomena between model scale and full scale are also influenced by scale effects, viscous effects and water quality. The influence of laminar-transition flow and Reynolds number difference between scales regarding generated pressure pulses is the second objective to be investigated.

In order to achieve the research objectives, the following studies have been conducted:

- Two high-skew propellers

  Numerical simulations regarding two high-skew model scale marine propellers mounted on inclined shaft were performed and pressure pulses under blade frequency were investigated. Simulations were conducted under different operating conditions J and cavitation numbers σ. Several meshes were generated systematically and used to perform a mesh dependency study. However, during the study massive sheet cavitation was predicted by numerical simulations both in Star-CCM+ and OpenFOAM while in the high speed videos recorded during experiments, these areas were only covered by intermittent sheet cavitation strips or bubble cavities. The discrepancies between cavitation patterns predicted numerically and observed experimentally lead to a significant difference regarding pressure pulses. Modifications of cavitation mass transfer model taking laminar separation into consideration for sheet cavitation inception was made for prediction

improvements.

- A conventional container vessel

  The studied case is the container vessel designed and studied in the VIRTUE and SONIC EU projects. In the experiments performed at HSVA, the model scale ship hull was put into the cavitation tunnel test section, thus the propeller was operating in the ship wake. Wake prediction was studied by several generated meshes for the ship hull region. Two meshes with/without blade tip refinement were considered to study tip vortex cavitation related phenomenon. Besides, two sets of configurations based on different scaling with different operating Reynolds numbers representing cavitation tunnel condition and towing tank condition are numerically considered. Both Star-CCM+ and OpenFOAM are used for all the simulated conditions as comparison and cross-reference. One of the research outputs from this study that could be highlighted is that the re-entrant jet and side-entrant jet of the sheet cavity plays an important role regarding the tip vortex cavitation bursting phenomena. Based on the monopole nature of bursting tip vortex cavitation, the isolated contributions of induced pressure pulses were studied which mainly concentrated in the BPFs ranging from 3^{rd} order to 10^{th} order.

- A general cargo vessel with LDP

  The third studied case is a general cargo vessel designed and studied in the LeanShips EU project which attempts to acquire maximum propeller efficiency by using a large diameter propeller incorporated by a new hull design with significantly reduced tip clearance. The tip clearance is about 1% of propeller diameter, which is much smaller than the typical choice of $20\% \sim 30\%$ of propeller diameter, and induced pressure pulse levels became one of the major concerns to be taken care of. Both model scale and full scale simulations are performed and the first four orders of BPF pressure pulses are predicted and compared to experimental measurements. Besides, the effect of hull roughness and free-surface are also studied.

For the cases that propeller is operating in behind condition, i.e. the container vessel and the general cargo vessel with LDP, hull pressure pulses in orders higher than 2^{nd} BPF are predicted and discussions regarding various reasons of RANS predicted higher order frequency pressure pulses are also included.

1.4 Thesis outline

The present thesis is divided into four parts. In `Chapter 1`, background information is introduced including discussions regarding the research needs, pressure pulse generation mechanisms, research methods, corresponding terminologies and research objectives.

In Chapter 2, descriptions of related numerical formulations and methodologies are presented including simulation tools, basic control equations, mass transfer cavitation model and transition sensitive turbulence model with its prediction of laminar separation.

In Chapter 3, the summary of the studied cases are presented. The first presented case corresponds to the typical configuration of the model scale marine propeller cavitation experiment and the pressure pulse induced by cavitation is studied especially with improved numerical model which includes the effect of laminar separation and sheet cavitation inception. The other two studied cases are presented following which are the container vessel and the general cargo vessel with LDP, while all of the two cases correspond to typical behind condition experimental configurations.

Lastly the summary of the thesis and possible future work are presented in Chapter 4.

2

Numerical modelling

2.1 Mass and momentum continuity equation

The basic control equations used in the present study are the mass and momentum continuity equations, and their formulation in RANS for incompressible flow is,

$$\frac{\partial \rho_m}{\partial t} + \nabla \cdot (\rho_m \mathbf{U}) = 0, \tag{2.1}$$

$$\frac{\partial \rho_m \mathbf{U}}{\partial t} + \nabla \cdot (\rho_m \mathbf{U}\mathbf{U}) = \nabla \cdot (\tau - \rho_m \overline{\mathbf{u}'\mathbf{u}'}) - \nabla p + F_s, \tag{2.2}$$

and the Boussinesq hypothesis is used for Reynolds stress tensor $\rho_m \overline{\mathbf{u}'\mathbf{u}'}$ modeling,

$$-\rho_m \overline{\mathbf{u}'\mathbf{u}'} = \mu_t (\nabla \mathbf{U} + (\nabla \mathbf{U})^T) - \frac{2}{3}\rho_m k \mathbf{I}, \tag{2.3}$$

where $\mathbf{U}$ represents time averaged velocity, $\mathbf{u}'$ represents the time-varying fluctuating component of velocity, μ_t is turbulent viscosity, F_s represents body forces, ρ_m for mixture density, τ represents averaged stress tensor and $\mathbf{I}$ represents identity tensor. Turbulent viscosity is modelled using the $k\omega - SST$ turbulence model as $\mu_t = \rho_m k T$ where T represents turbulent time scale and k represents kinetic energy. The turbulent time scale is calculated as $\min(a^*/\omega, a_1/SF_2)$ in which a^*, a_1 are model constants, F_2 is a blending function, S is the absolute value of the strain rate and ω represents specific dissipation rate. Both k and ω are modelled via additional Reynolds transport equations. The implementation of $k\omega - SST$ turbulence model in Star-CCM+ is based on [36] with S in the definition of the eddy viscosity instead of the vorticity and furthermore, Durbin's limiter in [37] is used where both modifications concern the calculation of T. In OpenFOAM the implementation is based on [38] with updated coefficients in [39].

Cavitation is one of the major sources of propeller induced pressure pulses. The single fluid linear mixture approach is used for the present multi-phase prob-

lem. The two phases water and vapor are represented by a volume fraction factor α which is between 0 and 1. Thus the mixture properties can be calculated as

$$\rho_m = \alpha_l \rho_l + (1-\alpha_l)\rho_v, \quad \mu_m = \alpha_l \mu_l + (1-\alpha_l)\mu_v, \quad \alpha_l + \alpha_v = 1,$$

in which the subscripts l and v represent liquid phase related quantities and vapor phase related quantities. The transport equation of the volume fraction is written as a pure convection equation with mass transfer source term for the liquid phase,

$$\frac{\partial \alpha_l}{\partial t} + \nabla \cdot \alpha_l \mathbf{U} = \frac{\dot{m}}{\rho_l}. \tag{2.4}$$

2.2 Schnerr-Sauer cavitation model

In reality, rather than a perfect purified medium, water contains many small bubbles which can break the water medium when under tension. The small vapor bubbles are commonly refered to as nuclei. The information of nuclei, including the distribution of numbers and sizes, could be determined experimentally, and usually it differs from test to test.

As indicated in 2.4, phase change is represented by a mass transfer source term. There are many cavitation mass transfer models available, and the Schnerr-Sauer cavitation model is one of the widely used models. For the study regarding marine propeller cavitation, the differences between different phase change modeling approaches are not significant [21]. In the Schnerr-Sauer cavitation model, the distribution of nuclei are assumed to be spherical and uniformly distributed in the water medium.

For uniformly distributed nuclei with diameter d and number n the volume in one unit can be estimated as in Equation 2.5, thus the volume fraction of nuclei can be expressed as in Equation 2.6 and bubble growth rates are estimated using a simplified Rayleigh relation as shown in Equation 2.7,

$$V_{nuc} = \frac{1}{6} n \pi d^3, \tag{2.5}$$

$$\alpha_{nuc} = \frac{V_{nuc}}{1+V_{nuc}} = \frac{\frac{1}{6} n \pi d^3}{1+\frac{1}{6} n \pi d^3}, \tag{2.6}$$

$$\frac{dR}{dt} = \sqrt{\frac{2}{3} \frac{p_{sat} - p_\infty}{\rho_l}}. \tag{2.7}$$

Accordingly the vapor production rate is calculated as,

$$\frac{d\alpha}{dt} = (1-\alpha) \frac{4\pi n R^2 \frac{dR}{dt}}{1+4\pi n R^3/3}. \tag{2.8}$$

The mass transfer source term on the right hand side of Equation 2.4 can be further re-organized as,

$$\frac{\dot{m}}{\rho_l} = \frac{\dot{m}}{\rho_l} - \alpha_l(\frac{1}{\rho_l} - \frac{1}{\rho_v})\dot{m} + \alpha_l(\frac{1}{\rho_l} - \frac{1}{\rho_v})\dot{m} = (\frac{1}{\rho_l} - \alpha_l(\frac{1}{\rho_l} - \frac{1}{\rho_v}))\dot{m} + \alpha_l(\frac{1}{\rho_l} - \frac{1}{\rho_v})\dot{m}, \tag{2.9}$$

while the first term in Eq. 2.9 on the right hand side can be decomposed into two terms (one for vaporization and one for condensation) as

$$\dot{m}_{ac} = C_c \alpha_l \frac{3\rho_l\rho_v}{\rho_m R}\sqrt{\frac{2}{3\rho_l}}\sqrt{\frac{1}{|p - p_{threhold}|}}\max(p - p_{threhold}, 0),$$

$$\dot{m}_{av} = C_v(1 + \alpha_{nuc} - \alpha_l)\frac{3\rho_l\rho_v}{\rho_m R}\sqrt{\frac{2}{3\rho_l}}\sqrt{\frac{1}{|p - p_{threhold}|}}\min(p - p_{threhold}, 0).$$

Then the total rate of mass transfer is modified accordingly as

$$\dot{m} = \alpha_l\dot{m}_{av} + (1 - \alpha_l)\dot{m}_{ac} = \alpha_l(\dot{m}_{av} - \dot{m}_{ac}) + \dot{m}_{ac}. \tag{2.10}$$

By introducing $\dot{V} = (\frac{1}{\rho_l} - \alpha_l(\frac{1}{\rho_l} - \frac{1}{\rho_v}))$ and $\frac{\partial u_i}{\partial x_i} = (\frac{1}{\rho_l} - \frac{1}{\rho_v})\dot{m}$, the final transport equation is written as,

$$\frac{\partial \alpha_l}{\partial t} + \nabla \cdot (\alpha_l \mathbf{U}) = (\nabla \cdot \mathbf{U} + \dot{V}_v - \dot{V}_c)\alpha_l + \dot{V}_c. \tag{2.11}$$

2.3 Laminar separation in the $\gamma - Re_\theta$ model

The transition sensitive turbulence model, $\gamma - Re_\theta$ model, is established based on the Local Correlation based Transition Modeling (LCTM) concept [41]. The model is based on empirical correlations and the used quantities are locally determined for general usage of parallel computation. The model links the flow transition characteristics (transition onset, length of transition, etc.) to flow features (pressure gradient, free stream turbulence intensity level, etc.) based on a series of two-dimensional experimental data. The model is coupled with the $k\omega - SST$ turbulence model with two additional equations. The first equation is the intermittency equation, which controls the production of kinetic energy inside the boundary layer; the second equation is a transport equation for transition momentum thickness Reynolds number, which is used to find the onset of transition and takes the non-local empirical correlations, transfers them into local qualities. Equation 2.12 displays the transport equation of intermittency γ, and Equation 2.13 the transport equation of momentum thickness Reynolds number $\widetilde{Re}_{\theta t}$ in Cauchy format,

$$\frac{\partial(\rho\gamma)}{\partial t} + \frac{\partial \rho U_j \gamma}{\partial x_j} = P_\gamma - E_\gamma + \frac{\partial}{\partial x_j}\left[\left(\mu + \frac{\mu_t}{\sigma_f}\right)\frac{\partial \gamma}{\partial x_j}\right], \tag{2.12}$$

$$\frac{\partial(\rho\widetilde{Re}_{\theta t})}{\partial t}+\frac{\rho U_j\widetilde{Re}_{\theta t}}{\partial x_j}=P_{\theta t}+\frac{\partial}{\partial x_j}\left[\sigma_{\theta t}(\mu+\mu_t)\frac{\partial\widetilde{Re}_{\theta t}}{\partial x_j}\right], \tag{2.13}$$

in which ρ denotes density, P and E are the production and destruction terms, μ is the molecular dynamic viscosity, σ_f and $\sigma_{\theta t}$ are model constants.

The foundation of this model is to use the correlation between scaled ratio of vorticity Reynolds number $Re_v=\frac{\rho y^2}{\mu}S$ and momentum thickness Reynolds number Re_θ to represent the boundary layer shape factor H,

$$\frac{\max(Re_v)}{2.193Re_\theta}\sim H. \tag{2.14}$$

Inside the boundary layer, y^2S, the product of squared wall distance and strain rate magnitude, can be regarded as the growth of disturbances, and the term μ/ρ can be regarded as its damping. Transition will be triggered when a critical value of Re_v is reached.

Especially, the model is able of predicting laminar-separation induced transition. In a laminar boundary layer, with the increase of adverse pressure gradient, the flow can be separating when shape factor H is higher than 3.5. Thus the scaling constant in 2.14 is changed to 3.235 for better accuracy in between the target shape factor range. In the original complete publication of the $\gamma-Re_\theta$ model in [40], the separation induced transition is formulated as

$$\gamma_{sep}=\min(s_1\max[0,\frac{Re_v}{3.235Re_{\theta c}}-1]F_{reattach},2)F_{\theta t}, \tag{2.15}$$

in which $s_1=2, F_{reattach}=e^{-(\frac{R_T}{20})^4}$ and the blending function $F_{\theta t}$ is used to control γ_{Sep} is only active inside the boundary layer. $F_{\theta t}$ is equal to zero in the free stream and one inside boundary layer, which is formulated as,

$$F_{\theta t}=\min(\max(F_{wake}\cdot e^{-(\frac{y}{\delta})^4}),1.0-(\frac{\gamma-1/c_{e2}}{1.0-1/c_{e2}})^2,1.0), \tag{2.16}$$

in which

$$\theta_{BL}=\frac{\tilde{Re}_{\theta t}\mu}{\rho U},\quad \delta_{BL}=7.5\theta_{BL},\quad \delta=\frac{50\Omega y}{U}\cdot\delta_{BL},$$

$$Re_\omega=\frac{\rho\omega y^2}{\mu},\quad F_{wake}=e^{-(\frac{Re_\omega}{1E5})^2}.$$

For the rest part of the model, the author refers to the publications in [41] and [40] and in [42] for cross flow instabilities.

2.4 Combination of laminar separation and cavitation

Unlike for full scale propellers, where surrounding flow can be regarded as fully turbulent, laminar and transitional flow is commonly found on blades of model

scale propellers. As introduced in chapter 1, it is generally believed that with Reynolds number higher than 1,000,000 the influence of laminar-transition effect of propeller generated forces are small, but removal of laminar-transition surface flow require way much higher Reynolds number [35]. Besides, many studies, including [43, 44, 45, 46, 47], revealed that in most conditions the sheet cavitation actually detach shortly downstream the location of laminar separation instead of from the minimum pressure point, with some exceptions with detachment inside the transition zone. At the same time, the problem is arising that there could be large discrepancies of cavitation pattern between numerical predictions and model scale experiments especially when operating under nearly uniform inflow conditions. As shown in the two international workshops on cavitation and propeller performance of International Symposium on Marine Propulsors [48, 49], the problem of over-prediction of sheet cavitation under certain conditions was found by different institute using various CFD packages, turbulence models, cavitation mass transfer models and nuclei properties in water medium.

In most Euler approach based cavitation mass transfer models, the sign of $(p - p_{sat})$ is used as the only or major vaporization indicator as the vaporization and condensation terms shown in section 2.2. Besides, one of the assumptions of the Schnerr-Sauer mass transfer model is the uniform initial distribution of nuclei, which is not true when the laminar boundary layer exists and nuclei may not penetrate into the boundary layer as in turbulent boundary layers. The Lagrangian method could be used to further study the problem as [50] regarding inceptions from nuclei with different diameters while the transition sensitive model has also been used to study the problem, including [51].

However, directly using transition-sensitive model do not really solve the problem as the predicted pressure distribution on the blades is hardly influenced, thus similar cavitation patterns would be predicted as with the fully turbulent turbulence models, even though the large area of laminar-transition region is predicted. Linking between transition sensitive turbulence model and cavitation mass transfer model is desired and the predicted laminar separation can be one candidate. One developing approach here is to calculate a laminar separation indicator which also multiples the two constants, C_c and C_v, which are the vaporization and condensation coefficients. This is somewhat desired since the two constants could be modified according to the user; while taking into consideration the fact that the laminar separation indicator would be modified to be one or zero, the original properties of the cavitation model could be maintained as much as possible.

One feature of the vorticity Reynolds number based transition models is that the transition always starts in the middle of the boundary layer, as γ and γ_{sep} in Equation 2.15 increase locally and act as source terms of turbulent kinetic energy k. The laminar separation indicator comes from γ_{sep} and fills the region between the middle boundary layer and the wall. Experiments performed in [43] regarding the NACA 16012 hydrofoil with 3 degrees angle of attack is used as a validation case here. Figure 2.1 shows numerical predicted laminar separation regions. The upper frame marks the region which satisfies Equation 2.15 while the lower frame

shows the modified separation indicator. The laminar separation could be found about 0.78 chord length which agree well with experimental observation. For the cavitating condition, numerical predictions using the original model ($\gamma - Re_\theta$ and Schnerr Sauer model) and the modified model ($\gamma - Re_\theta$ and modified C_c and C_v with *SepInd* in Schnerr Sauer model) are shown at inception time (T = 0.002s) and developed time (T = 0.1s) as in figure 2.2. The inception of sheet cavity was found from the foil rear part and moves upstream with the appearance of sheet cavity, and finally an equilibrium state was found upstream foil mid chord. This general behavior agrees well with experimental observations.

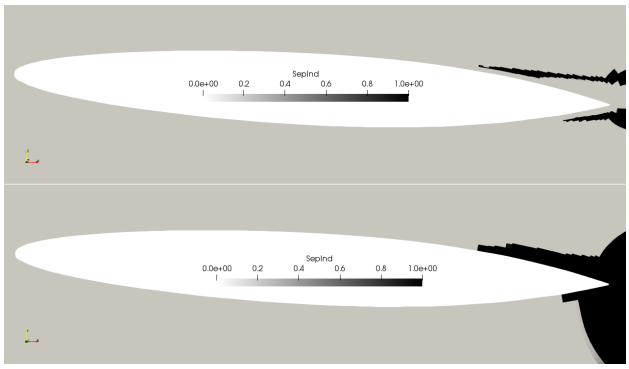

Figure 2.1: The laminar separation indicator, upper frame: original prediction based on γ_{sep}; lower frame: modified separation indicator. NACA 16012, AoA = 3 degrees, *Re* = 300,000, σ = atm.

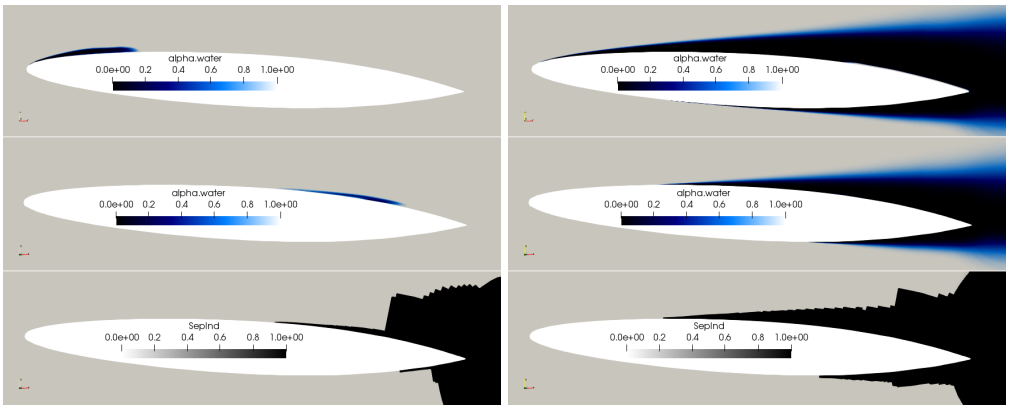

Figure 2.2: Numerical predicted cavitation patterns and separation indicator at 0.002s (left column) and 0.1s (right column).From top to bottom: predictions using original model; predictions using modified model; separation indicator predicted by modified solver. NACA 16012, AoA = 3 degrees, *Re* = 1,000,000, σ = 0.045.

2.5 Simulation Tools

Two major packages are used in the present study, which are the open-source package OpenFOAM and commercial package Star-CCM+. In both codes, the set of equations is solved in a segregated manner, i.e. the equations of different quantities are solved by sequence and iterations are needed until convergence. In OpenFOAM, the solver `interPhaseChangeFoam` is used for two incompressible, isothermal immiscible fluids with phase-change and transport equation of volume fraction (TEM) is used to model the phases distribution. In the present study, a modified code based on `interPhaseChangeFoam` implemented into OpenFOAM v1806 is used. Simcenter Star-CCM+ is a complete multiphysics simulation tool and in the present study the versions 11.06.010 and 12.06.010 were used. Same as with OpenFOAM, for the presented simulated cases, the fluid is assumed to be incompressible, isothermal immiscible and TEM is used for volume fraction capturing. For simulations concerning water-air free surface, the VOF method is used.

Throughout the simulations performed in the thesis, implicit second order upwind Euler scheme is used in both OpenFOAM (referred to `backward`) and Star-CCM+ (referred to `second order`) while the implicit backward Euler with first order accuracy, referred to as `Euler` in OpenFOAM and `Euler implicit` in Star-CCM+, is used for simulation initialization for most cases. Gauss theorem is used for the calculation of cell-centered gradient terms and convection terms as well as Laplacian terms in OpenFOAM while in Star-CCM+ the calculation of gradient terms are hybrid with least-squares methods. Specificlly regarding gradient calculation in OpenFOAM, linear interpolation scheme of face value is always used without limiters while in Star-CCM+ the interpolation relies on reconstruction gradients with Venkatakrishnan limiter. Regarding convection flux calculation for term $\nabla \cdot (\rho \mathbf{U}\mathbf{U})$, interpolation of $\mathbf{U}_f$ uses two schemes, where 2^{nd} order upwind differencing is the first one, denoted as `linear upwind` in OpenFOAM and `second order` in Star-CCM+ while again in Star-CCM+ the reconstruction gradient is used. A less diffusive TVD (Total Variation Diminishing) scheme `limitedLinear` is also used for certain cases in OpenFOAM. First order upwind scheme is used for turbulent terms and volume fraction factor α as suggested in [52]. Pointwise is the major package for mesh generation while Star-CCM+ build-in meshers might also be used if simulations are performed only in Star-CCM+. Regarding pressure velocity coupling, the SIMPLE algorithm is always used for steady-state simulations and transient simulations in Star-CCM+. In OpenFOAM the PIMPLE algorithm is used for transient simulations.

3

Simulation results

3.1 Two high-skew propellers

General description

In this study, two high-skew model scale marine propellers are considered. The two propellers have similar designs and propulsion characteristics while one is slightly more tip unloaded than the other one. Thus it is interesting to investigate the design influence on the cavitation phenomenon and pressure pulses both experimentally and numerically. The geometries are shown in figure 3.1 including surrounding grids.

Experiments were performed in the cavitation tunnel T31 at Kongsberg Hydrodynamic Research Centre at Kristinehamn, Sweden. The propeller shaft was inclined about 10 degrees to create blade load variations. The propellers were tested under different advance ratios and cavitation numbers. Eight pressure transducers were placed on the top wall of the cavitation tunnel test section above the propeller to measure induced pressure pulse levels. High speed videos were recorded for detailed study of related cavitation phenomenon. Experimental measurements show that only the blade harmonic frequency pressure pulses are significant and those in higher order harmonics are small enough to be neglected. Numerical prediction and results comparison will be shown in the following section and more details can be found in paper A.

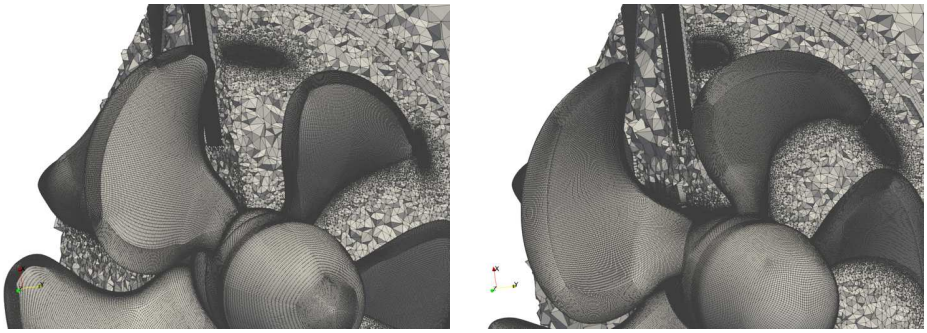

Figure 3.1: Geometry and meshes of propeller A (left) and propeller B (right)

Results

Non-cavitating condition pressure pulses were numerically predicted and results agreed well compared to experimental measurements both predicted by OpenFOAM and Star-CCM+ using RANS with $k\omega - SST$ turbulence model, as shown in figure 3.2 and figure 3.3. A mesh study was performed using Star-CCM+ and it shows the pressure pulse prediction for the current configuration is not highly mesh dependent, since a mesh with a propeller region of 3.6 million cells (mesh C in figure 3.3) predicted similar results compared to a 26.3 million cells mesh (mesh OFF in figure 3.3).

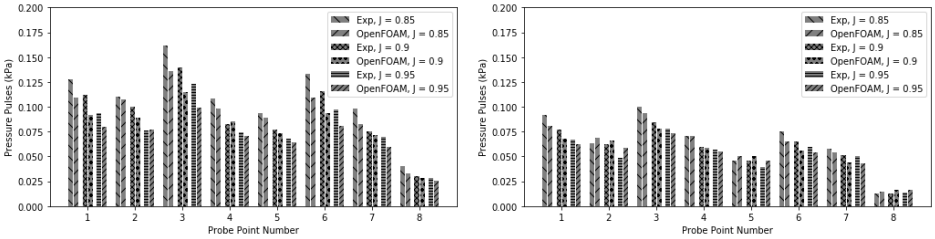

Figure 3.2: OpenFOAM results, 1^{st} BPF pressure pulses, non-cavitating , propeller A (left) and propeller B (right)

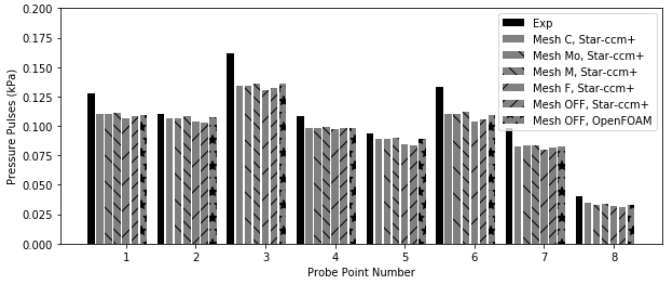

Figure 3.3: Predicted pressure pulse levels by different meshes, $J = 0.85$, non-cavitating, propeller A

However, for the cavitating conditions, massively over-predictions of sheet cavitation could be found on both propellers and the predicted pressure pulses are rather different compared to experimental measurements, not only absolute values but also the spatial distributions on the transducers. As observed in the experiments, for propeller A under condition $J = 0.85$ and $\sigma = 2.0$, the sheet cavitation mostly develop at the tip leading edge, while traveling bubble cavitation could form without any attached sheet cavitation. These typical patterns are shown in figure 3.5. In the numerical predictions as shown in figure 3.4, the blade suction side is covered by sheet cavitation which is clearly different from experimental observations.

The arising problem that sheet cavitation might be over predicted has been discussed both in Chapter 1 and Chapter 2. By studying numerical simulations performed by other researchers' over-prediction results, the area of over-prediction of sheet cavity is usually reflected as bubble cavitation observed in experiments. The bubble cavitation reveals the fact that local pressure drops below saturation pressure since certain nuclei could develop while for some reason sheet cavity couldn't develop on the blade surface. This type of isolated on blade bubble cavitation is not considered to appear in full scale, indicating this is a model scale phenomenon.

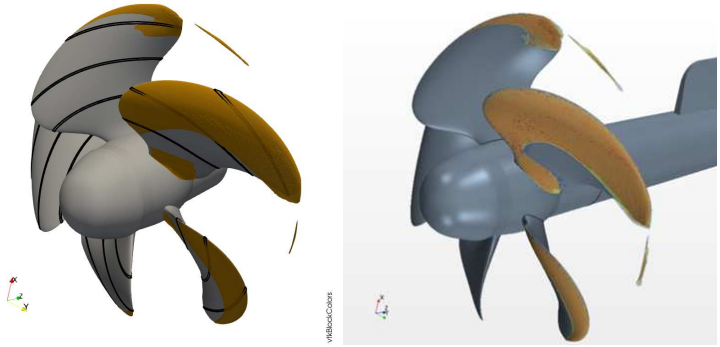

Figure 3.4: Predicted cavitation pattern for propeller A with $J = 0.85$, $\sigma = 2$ by OpenFOAM (left) and Star-CCM+ (right)

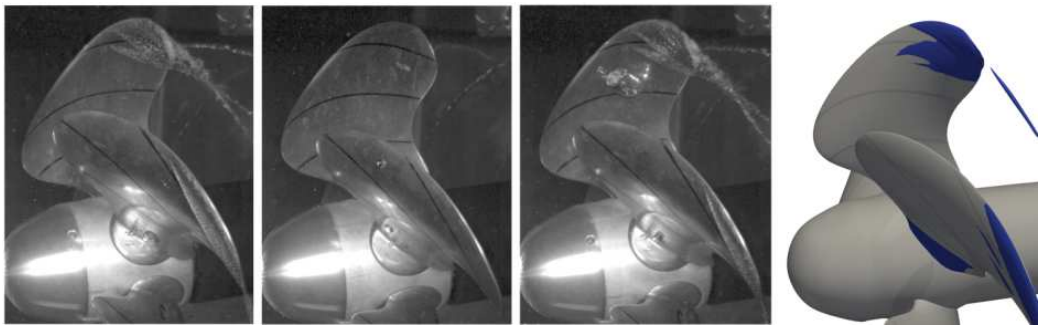

Figure 3.5: Cavitation patterns from high speed videos, propeller A, $J = 0.85$ and $\sigma = 2$; frame 1, 2, 3: snapshots from experimental recordings; frame 4: numerical prediction using improved model

The transition sensitive turbulence model, $\gamma - Re_\theta$ model was used to perform further investigation. For non-cavitating conditions, different free-stream turbulence levels were considered and improved propulsion coefficients were predicted. Large regions of laminar-transition zone were predicted on the blade suction side and especially, series of near-wall streaky disturbances in the boundary layer which triggers transition to turbulence were predicted, as shown in figure 3.6. These near-wall disturbances also indicate that the criteria $\frac{Re_v}{3.235 Re_{\theta c}} > 1$ is locally fulfilled as shown in figure 3.7. Though the predicted difference of thrust coefficient differs up to about 4% between the $k\omega - SST$ turbulence model and $\gamma - Re_\theta$ transition model, not much difference could be found regarding non-cavitating conditions 1^{st} BPF pressure pulse levels.

Thus the predicted separation indicator *SepInd* is linked to the cavitation model as discussed in Section 2.4 and significant improvements could be found regarding predicted cavitation patterns as shown in figure 3.5.

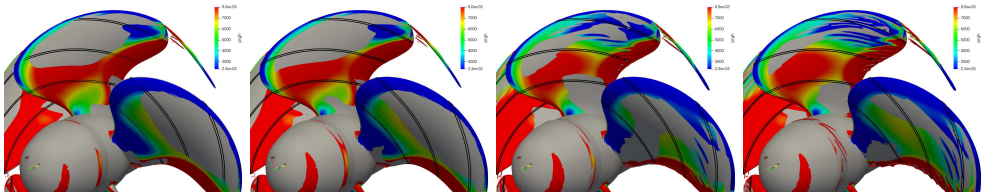

Figure 3.6: Iso-surface of Q = 4e6, propeller A

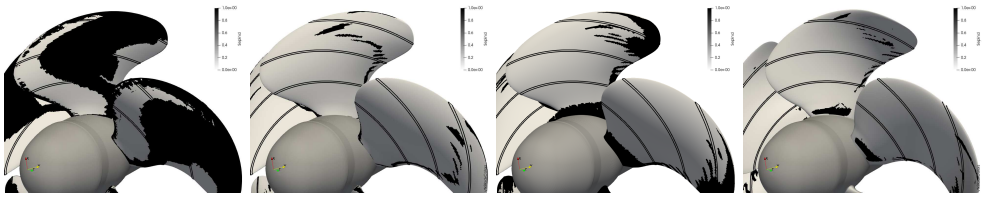

Figure 3.7: Laminar separation indicator with non-cavitating flow and $J = 0.85$, propeller A with $Tu = 5\%$, $Tu = 0.5\%$, $Tu = 0.1\%$ and propeller B with $Tu = 0.1\%$

3.2 A conventional container vessel

General description

This study focuses on the numerical prediction of cavitation and pressure pulse induced by a model scale marine propeller operating in behind hull conditions.

The studied case is the container vessel used in the VIRTUE (The Virtual Tank Utility in Europe) and SONIC (Suppression Of underwater Noise Induced by Cavitation) EU projects. The container vessel is a representative 3600 TEU standard container vessel developed in 2002 with a bulbous bow and single five-bladed high skew fixed pitch propeller.

Experiments were performed in the cavitation tunnel HYKAT at HSVA, Germany, which is large enough for the installation of the whole ship model. Pressure fluctuations were measured at 13 probe points via pressure transducers mounted on the ship hull above the propeller. The pressure transducer arrangements are shown in figure 3.8.

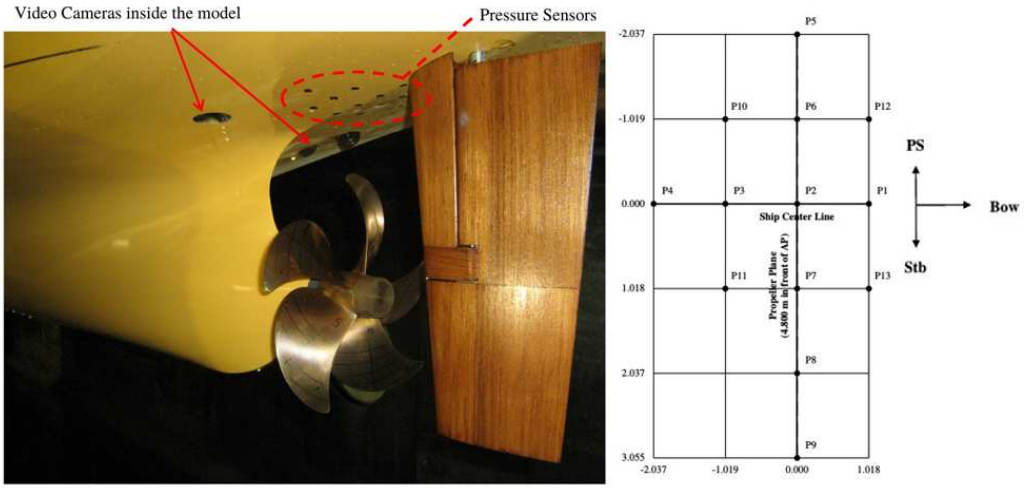

Figure 3.8: Pressure transducer arrangements on the model scale ship hull

A mesh dependency study was performed first and comparison between different meshes show that the wake is highly dependent on the ship hull mesh, especially regarding prism cell layer generation. After the determination of ship hull mesh, the behind-condition simulations including the propeller were carried out. Two scaled model conditions were considered, where condition 1 corresponds to cavitation tunnel condition and condition 2 corresponds to a towing tank condition. Two propeller meshes were considered with/without blade tip refinement in order to investigate tip vortex related phenomena. Both OpenFOAM and Star-CCM+ were used for all the simulated conditions. The used meshes are shown in figure 3.9 and 3.10. More details can be found in the appended paper B.

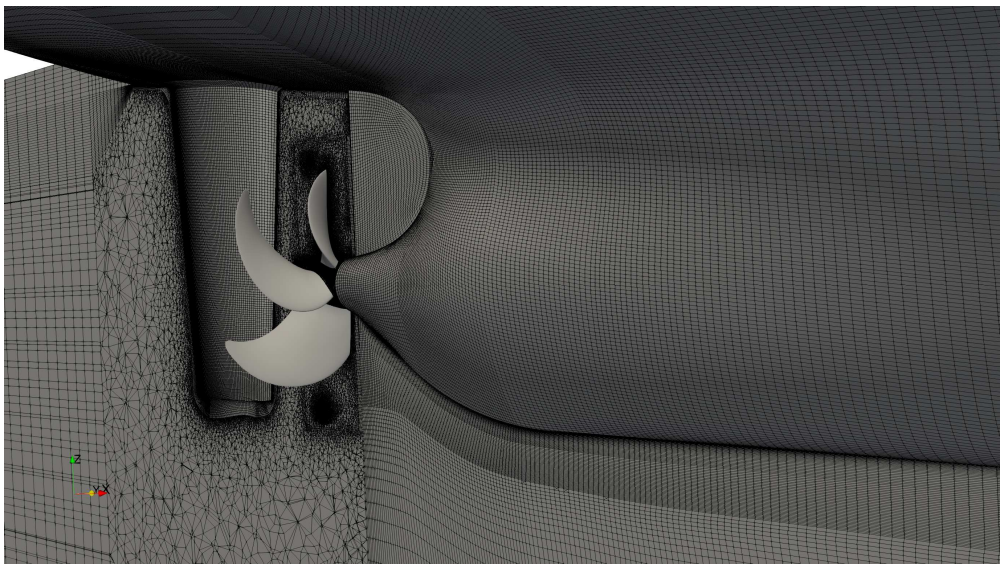

Figure 3.9: Mesh close to the aft body

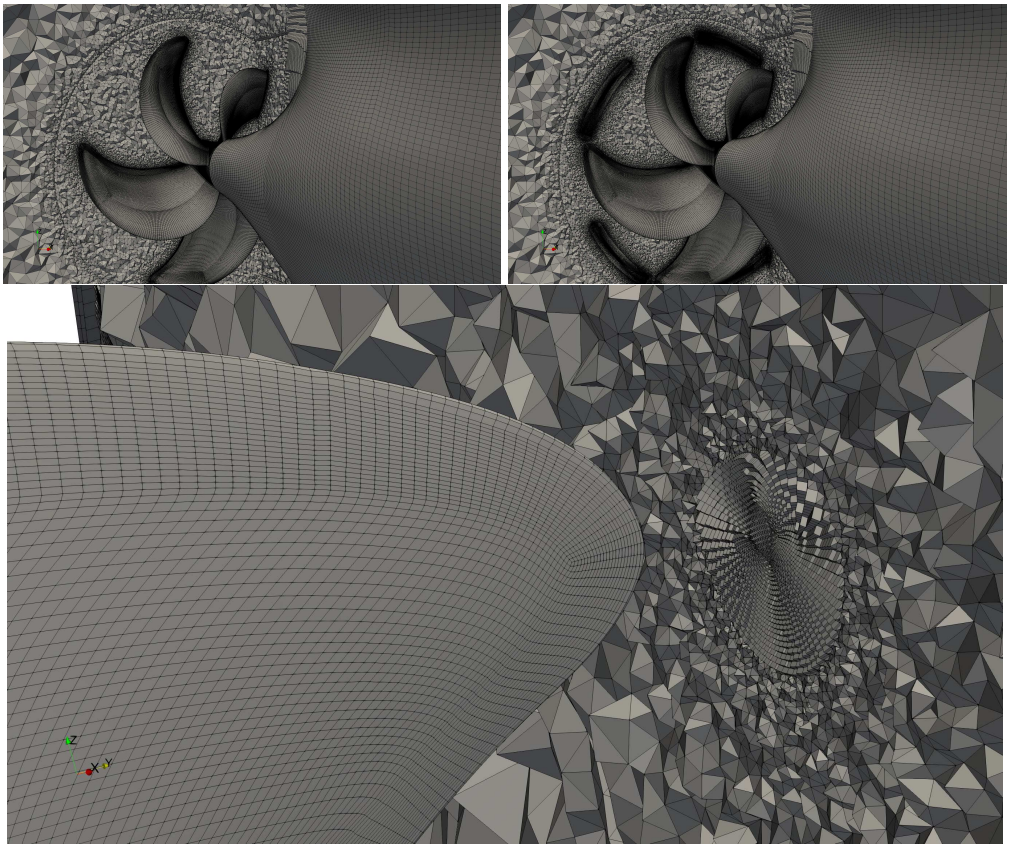

Figure 3.10: Mesh view close to the propeller of base mesh; tip refined mesh and closer view of tip refinement region.

Simulation results

For non-cavitating conditions, the predicted pressure pulses and comparison with experimental measurements are summarized in figure 3.11. The predicted model scale pressure are scaled to full scale values where the K_p is calculated using model scale values and K_p is assumed to be constant between different scales,

$$K_p = \frac{\hat{p}_m}{\rho_m n_m^2 D_m^2}, \quad \hat{p}_s = K_p \rho_s n_s^2 D_s^2. \tag{3.1}$$

The values are concentrated in the blade passing frequency and numerical predictions generally agree with experimental measurements. At some probe points there are over-predictions of about $30\% \sim 40\%$ but the maximum difference in absolute value is small, about 0.4 kPa in full scale.

The predicted non-cavitating pressure pulse levels show very small differences regarding the two operating conditions, though the Reynolds number differs about $3 \sim 4$ times. The prediction difference between the two numerical packages is also very small, even though the numerical algorithms and discretization schemes are not the same. Besides, using the tip refined mesh, much stronger tip vortex was predicted, but there is little difference regarding predicted pressure pulse levels compared to the predictions using the base mesh.

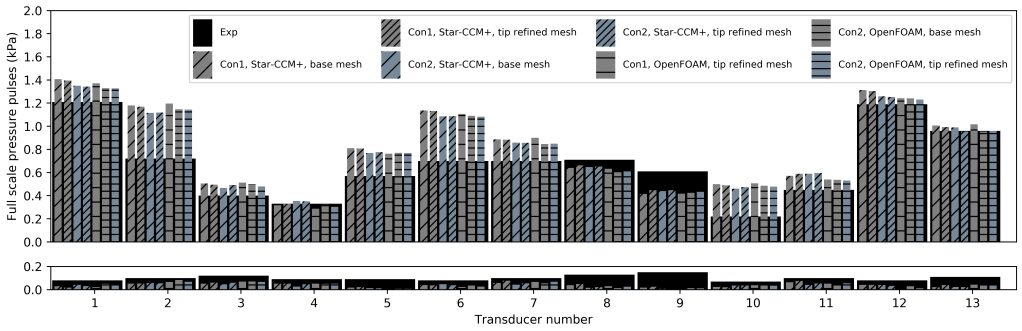

Figure 3.11: 1^{st} (upper frame) and 2^{nd} (lower frame) orders of BPF pressure pulse levels

The prediction of cavitation patterns agree well compared to observations in the experiments, including the convex shape of sheet cavity and its development as well as sudden attenuated tip vortex cavitation with secondary structures predicted by the tip refined mesh, though the stream-wise extent of the tip vortex cavitation is weaker compared to experimental observations. The predicted cavitation patterns and comparison to experimental recordings are shown in figure 3.12.

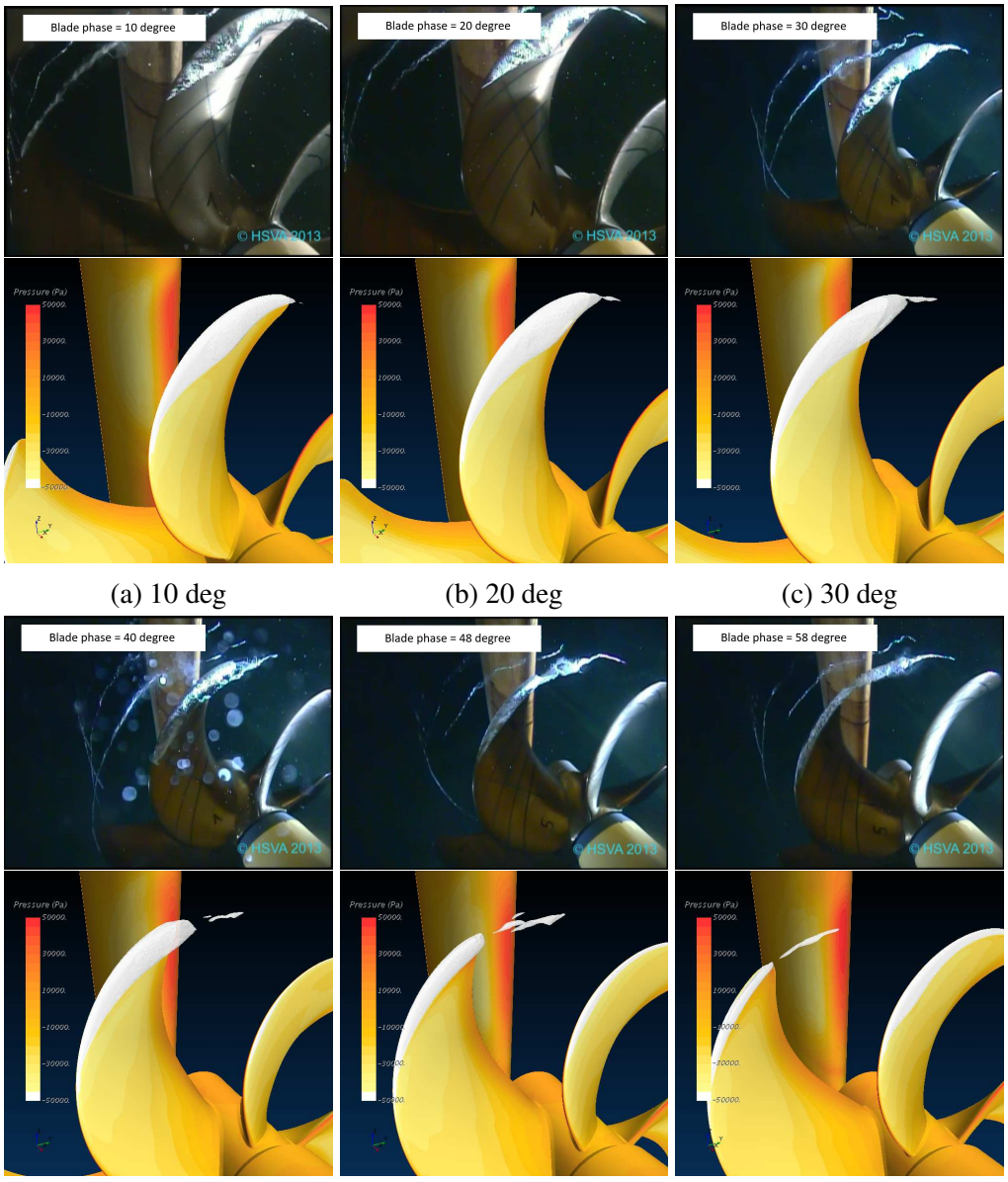

(a) 10 deg (b) 20 deg (c) 30 deg

(d) 40 deg (e) 48 deg (f) 58 deg

Figure 3.12: Predicted cavitation pattern and comparison with experimental recording

Experimental recordings show that the sheet cavitation is the pronounced cavitation phenomenon. The sheet cavity interface is sharp and clear while a convex vapor structure could be found moving from the blade leading edge to the blade trailing tip, originate at the blade position where the sheet cavity starts to form. The sheet cavity decreases after blade position of 40 degrees. Around 40 to 48 degrees, coincident to the time when the convex vapor structure travels to the blade tip end, the tip vortex cavitation starts to develop significantly and become quite unstable and bursting with rather complex flow dynamics. After that, the tip vortex cavitation is back to a relatively stable state around 58 degrees.

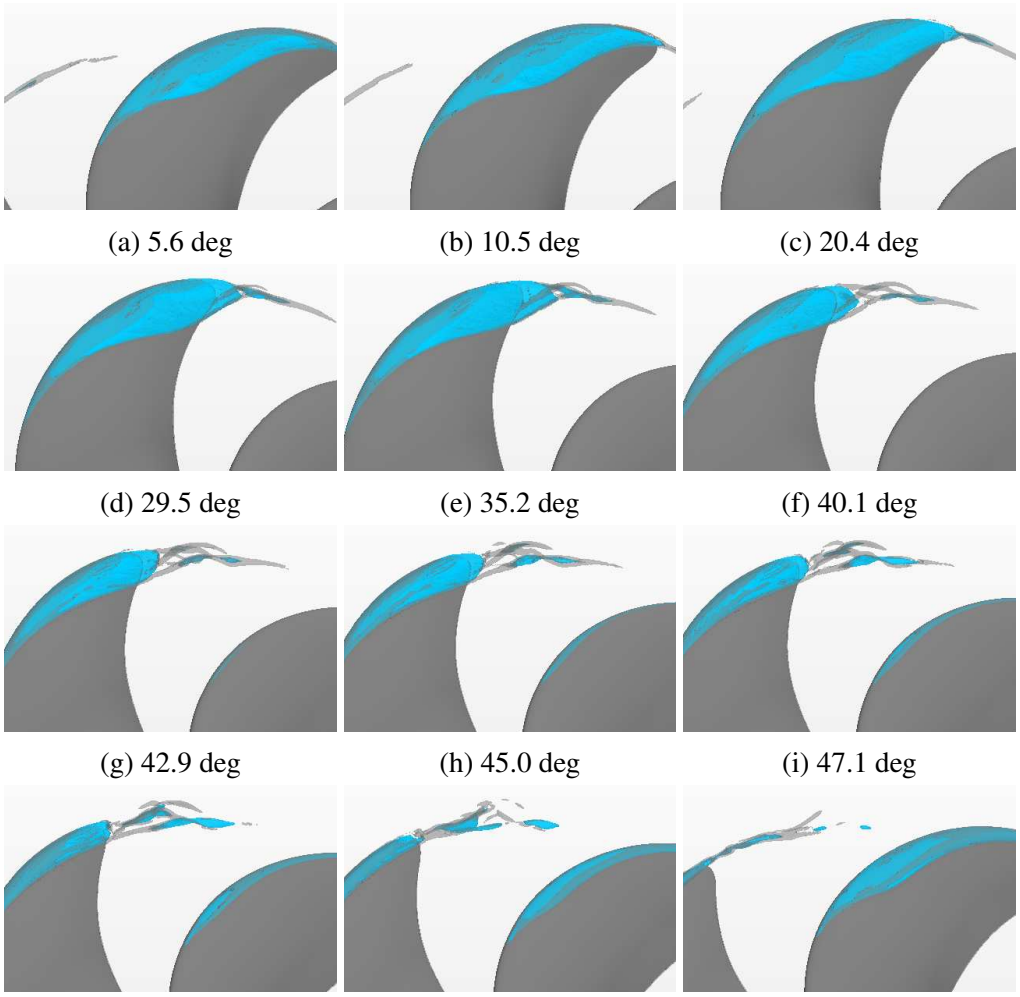

(a) 5.6 deg (b) 10.5 deg (c) 20.4 deg

(d) 29.5 deg (e) 35.2 deg (f) 40.1 deg

(g) 42.9 deg (h) 45.0 deg (i) 47.1 deg

(j) 49.9 deg (k) 54.8 deg (l) 64.7 deg

Figure 3.13: Predicted iso-surfaces of α=0.5 and Q=1e7 for condition 1 with tip refined mesh

Transparent cavitation patterns together with the iso-surfaces of $Q = 1 \times 10^7$ for condition 1 are shown in figure 3.13, to show the development of tip vortex, tip vortex cavitation, sheet cavitation and their interactions. There is a jet flow formed at about 0 degrees where the sheet cavity starts to develop, deduced from the last frame (-7.3 degrees) and the first frame (5.6 degrees). Before the jet flow reaches the tip region, say earlier than 30 degrees, the tip vortex is very stable and limited tip vortex cavitation could be found developing. Then the secondary vortex structures start form and the tip vortices, as well as tip vortex cavitation, become quite active around blade phase of 48 degrees, which correspond to the time when the jet flow arrives at the blade tip end. Instead of a main tip vortex structure, the iso-surfaces of Q criterion show that the tip vortex is decomposed into several rolling structures. The secondary structures starts to cavitate which lead to a complex flow field.

The prediction of induced pressure pulse levels agree well for condition 1 including satisfying predictions of 1^{st}, 2^{nd} and 3^{rd} BPFs but over-predictions could be found for the 4^{th} and 5^{th} BPFs. The higher order BPF pressure pulses levels are around 0.5 kPa $\sim$ 1.0 kPa in experiments and 0.5 $\sim$ 2.5 kPa in numerical predictions. The results are shown in figure 3.14 to figure 3.16. Differences were found between the two scaled conditions and the major difference is the predicted larger sheet cavitation extent which leads to higher 1^{st} order BPF pressure pules in condition 2.

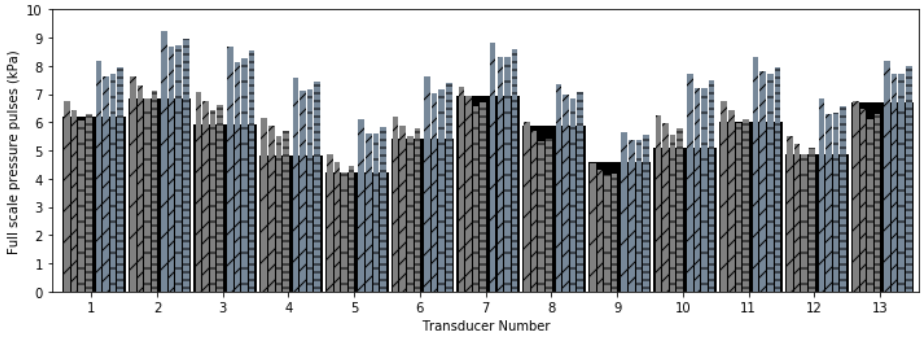

Figure 3.14: 1^{st} order BPF pressure pulse levels

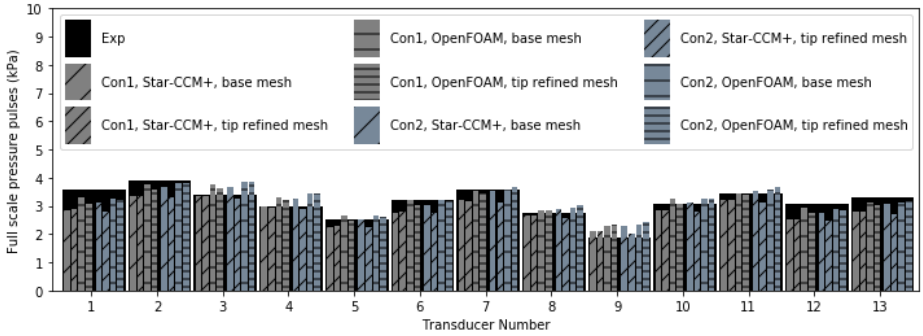

Figure 3.15: 2^{nd} order BPF pressure pulse levels

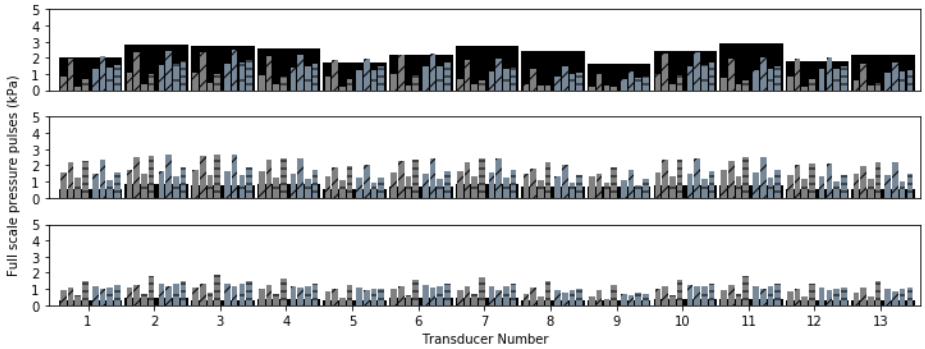

Figure 3.16: 3^{rd} to 5^{th} orders BPF pressure pulse levels

As shown in figure 3.17, the probed values of non-dimensional pressure (K_p) located at transducer 2 in three blade passing period predicted using Star-CCM+

are presented for both base mesh and tip refined mesh under the two operating conditions. The prediction results in condition 1 are plotted in black lines and red lines are used for condition 2. The magnitudes of the predicted non-dimensional pressure signals in condition 2 are larger than in condition 1 while the signal fluctuations are of similar magnitudes. This is in accordance with the FFT results that the 1^{st} order BPF pressure pulses are larger in condition 2 while the values are less influenced for the rest order of BPFs. The major events in the signals are similar for one blade passing for the two operating conditions: starting from 0 degree, the signals decrease until about 30 degrees, after that a rapid increase and decrease can be found which forms the first signal peak at around 40 degrees, then follows the second peak at around $50 \sim 60$ degrees and lastly the signal decrease with fluctuations and the signal repeats. For the pressure signals predicted using the base mesh, the second pressure peak is absent and the first pressure peak is stronger and ends earlier.

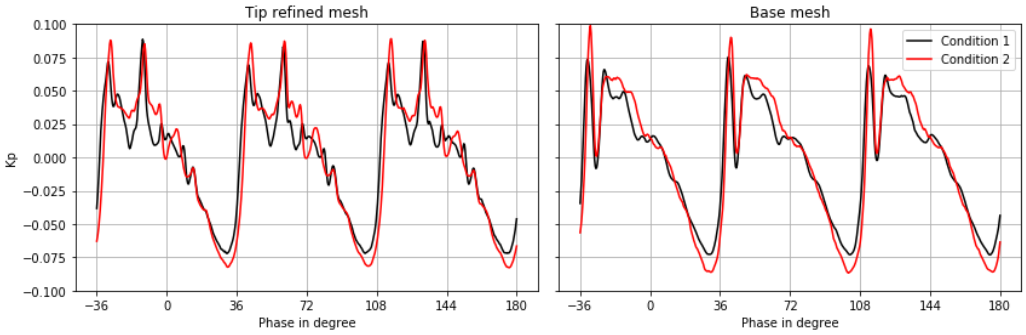

Figure 3.17: Non-dimensioned pressure history of probe 2

Vapor volumes were recorded during the numerical simulations as $V_{vapor} = \Sigma \alpha_{v,i} V_i$. It is also of interest to isolate the vapor volume of the sheet cavitation and the tip vortex cavitation, thus the cells with wall distance less than 2 cm, which covers the sheet cavitation but excludes the tip vortex cavitation, are selected and the vapor volume of these cells are computed as inner vapor volume. Taking second derivatives over time of the recorded vapor volumes results in the vapor rate shown in the first frame of figure 3.18. The resulting curves have highly similar shapes compared to the pressure signals. It could be calculated that for this probe, the pressure fluctuation is about $\hat{p} \sim 2313.71 \times d^2V/dt^2$. The calculated tip vortex cavitation volume rate is shown in the second frame of figure 3.18, and the deduced pressure pulse levels induced by TVC are calculated, as shown in figure 3.19. Taking advantage of the linear relationship, the vapor volume in the blade tip region was isolated and this procedure indicates that the tip vortex cavitation and the secondary cavitation structures induced pressure pulses up to 10^{th} BPF.

The analysis of vapor volumes and pressure fluctuations provides a more complete picture of the pressure pulse mechanisms for the present case, which is one of the common types could be found in behind conditions. Starting from 0 degrees, the present blade sheet cavitation extent increases until the total vapor volume

reaches its maximum at around 30 degrees. At the same time, the jet flows form at around mid chord and travels to the blade tip. Then the sheet cavitation starts to decrease in extent and pressure starts to increase. During this process the tip vortex cavitation develops steadily. At about 40 degrees the jet flows reaches the blade tip end, which leads to that a part of the sheet cavity collapses. After the collapse, the pressure bounces back to relatively higher values, which is the first pressure peak observed in the pressure signals. This event is less pronounced for a tip refined mesh, due to the fact of tip vortex cavitation development. The blade tip flow is influenced by the entrance of jet flows. Violent growth and collapse of tip vortex cavitation could be observed between 48 degrees to 54 degrees, which lead to the second pressure peak. After the second peak, the tip vortex cavitation shows a monopole breathing manner and induce a series of fluctuations till about 82 degrees, added to the decreasing pressure signals. The tip vortex cavitation related phenomenon generate pressure pulses in higher order BPFs, while the jet flow related sheet cavity collapse would lead to transient pressure fluctuations which is another mechanism contributing to higher order BPF pressure pulses generation.

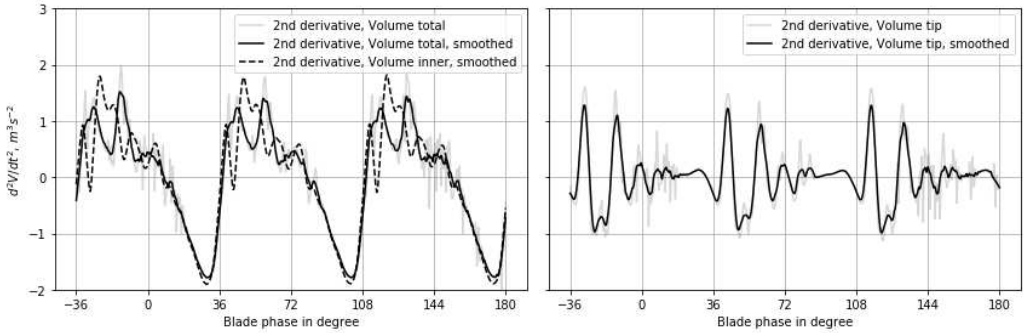

Figure 3.18: Cavity acceleration calculated based on recorded cavitation volumes

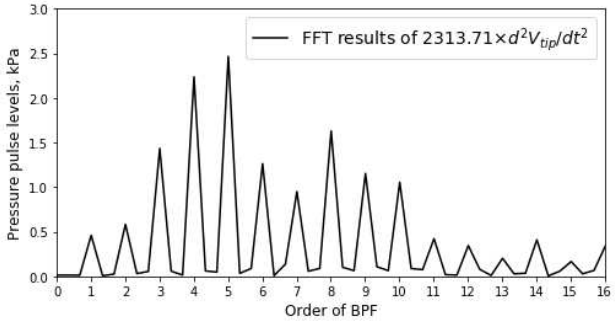

Figure 3.19: FFT result of equivalent pressure pulse based on d^2V_{tip}/dt^2

The generation and collapse of tip vortex cavitation is repeated even outside the wake peak, as shown in figure 3.20. Especially in the last four frames, at 73.4 degrees, the two tip vortex cavitation segments are collapsing, while the segment

between them are emerging at 75.5 degrees and 80.4 degrees and finally collapse at 82.5 degrees. However, this phenomenon could not be observed in the experimental recordings. In the experiments, the extent of tip vortex cavitation is continuous and maintains its shape significantly further downstream, but the stretching shape could be seen clearly.

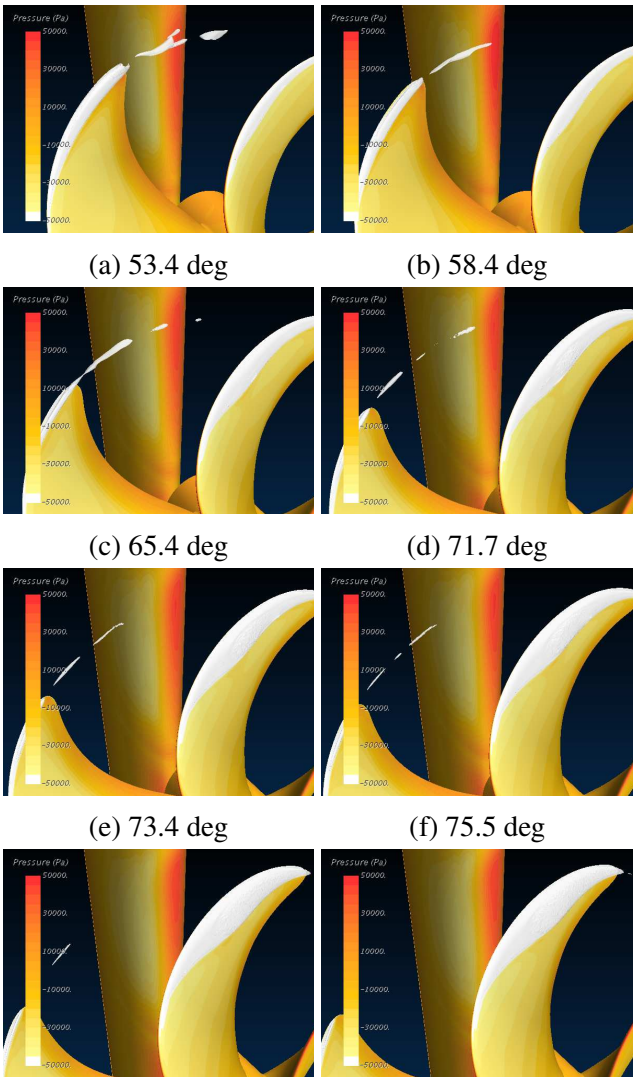

(a) 53.4 deg (b) 58.4 deg

(c) 65.4 deg (d) 71.7 deg

(e) 73.4 deg (f) 75.5 deg

(g) 80.4 deg (h) 82.5 deg

Figure 3.20: Tip vortex collapse and rebounding

3.3 A general cargo vessel with LDP

General description

The studied case here is a ship with LDP (Large Diameter Propeller) designed in the LeanShips (Low Energy And Near to zero emissions Ships) project. The extremely low tip clearance ($\sim 1\%$) makes a higher efficiency propulsion system come true but clearly the effect of induced hull pressure pulse needs to be assessed.

Several conditions were considered in this study, as summarized in Table 3.1, here named Condition A, B1, B2, and C. The model scale experiments were carried out in the DWB (Depressurized Wave Basin) at MARIN (Maritime Research Institute Netherlands) and induced pressure pulses were recorded via 14 pressure transducers. The views of meshes are shown in figure 3.21 and the arrangement of pressure transducers in figure 3.22.

Conditions	Scale	Free surface	Wall roughness
A	Model	no	Smooth
B1	Full	no	Smooth
B2	Full	no	Rough (120 micrometers)
C	Full	yes	Rough (120 micrometers)

Table 3.1: Summary of simulation conditions

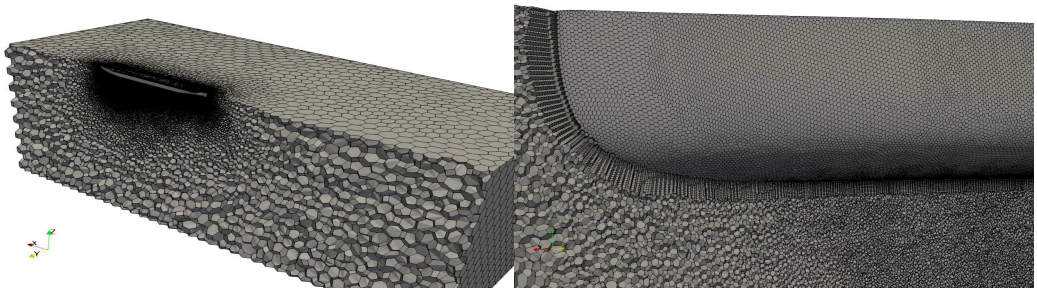

(a) Simulation domain for condition B

(b) Volume mesh close to the forebody

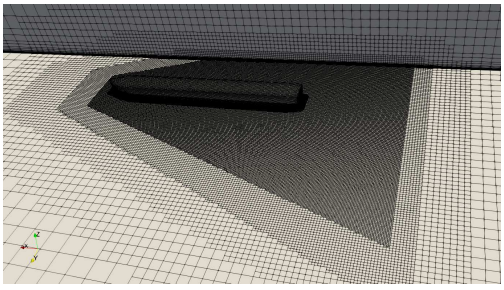

(c) Free surface mesh for condition C

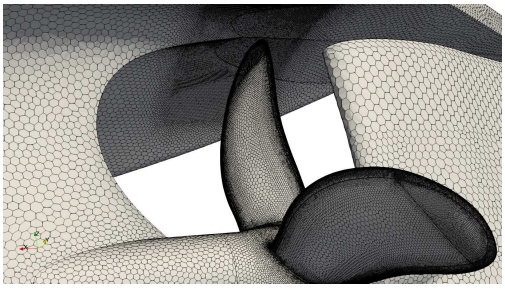

(d) Propeller and aft-body surface mesh

Figure 3.21: Views of generated volume mesh

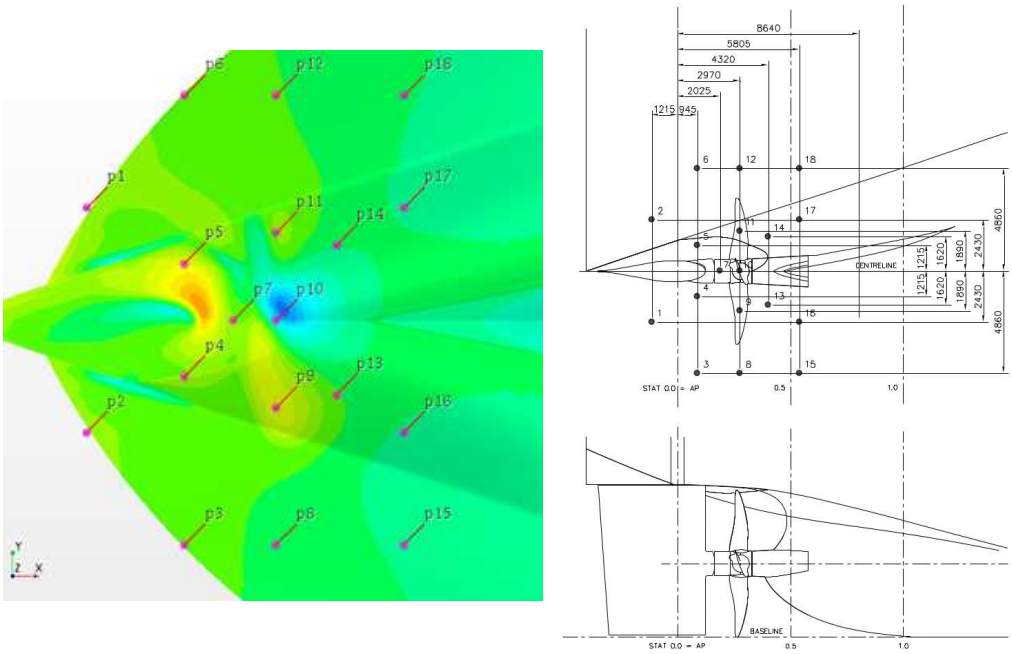

Figure 3.22: Arrangement of pressure transducers

Simulation results

For conditions A, B1 and B2, the predicted non-cavitating thrust and torque coefficients are shown in figure 3.23. The match with experimental data is rather satisfying for the thrust prediction, and the relative difference of predicted mean thrust coefficients compared to experimental data are 1.2%, −2.5% and −0.1% respectively. For the torque predictions, the relative difference of predicted mean coefficients compared to experimental data are 4.9%, 1.6% and 3.1% respectively.

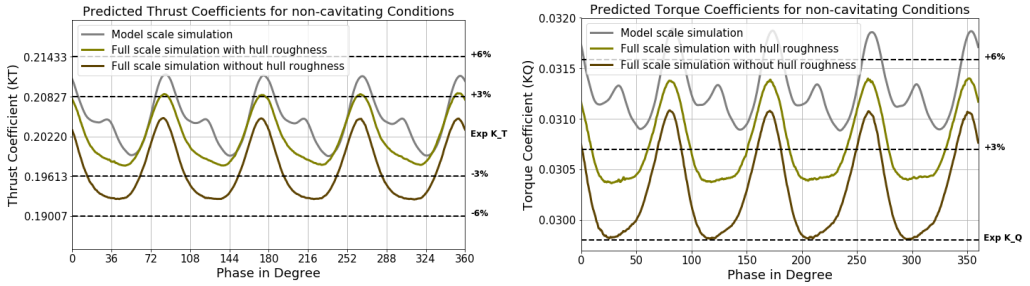

Figure 3.23: Predicted thrust and torque coefficients for non-cavitating conditions

The predicted pressure levels for selected points in full scale for these non-cavitating conditions are shown in figure 3.24. Together with probed pressure fluctuation signals (scaled to K_p) in figure 3.25, it is found that the propeller suction side is responsible for transient pressure peaks and the transient peaks lead to higher order components after FFT.

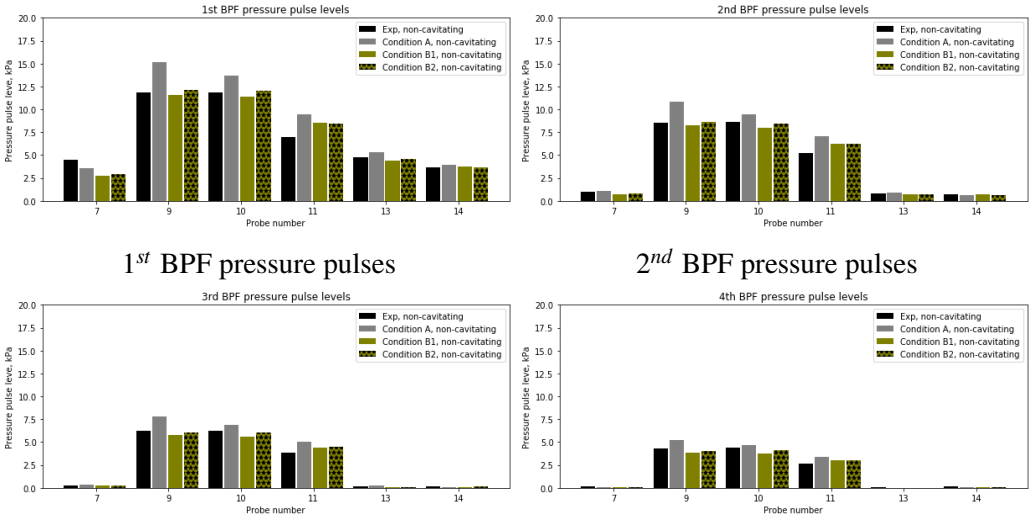

1^{st} BPF pressure pulses 2^{nd} BPF pressure pulses

3^{rd} BPF pressure pulses 4^{th} BPF pressure pulses

Figure 3.24: Pressure pulse levels at selected locations, non-cavitating condition

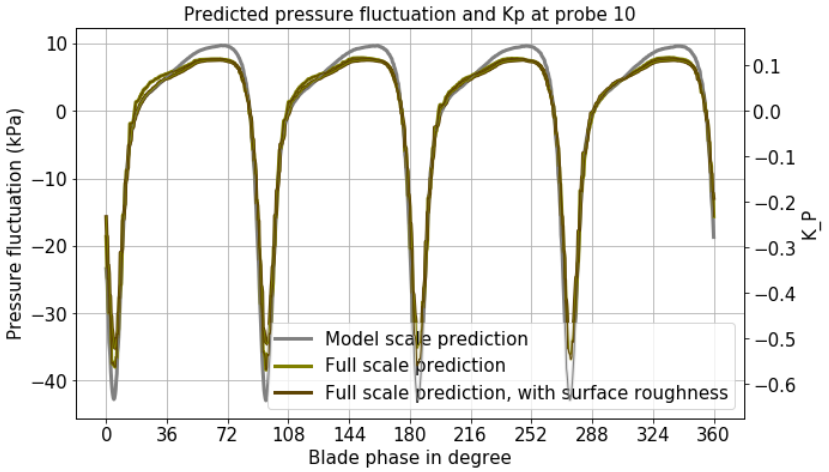

Figure 3.25: Predicted pressure fluctuation and K_p at probe No. 10

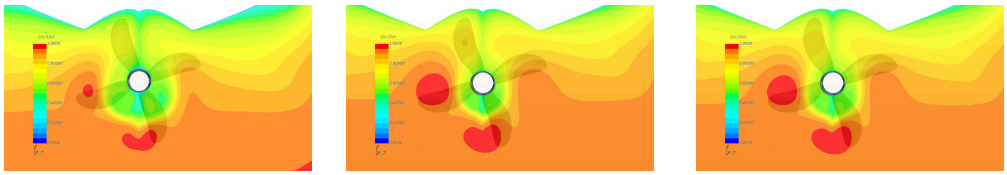

(a) Condition A (b) Condition B1 (c) Condition B2

Figure 3.26: Effective wake at blade phase of 22.5 degrees under different conditions

The pressure pulse differences between conditions are directly related to the wakes the propeller is operating in. The boundary layer is comparably thicker

in model scale than in full scale, while the hull roughness also leads to a thicker boundary layer. The effective wakes under the conditions are shown in figure 3.26. Together with the pressure signals in figure 3.25, it is found that the difference of wakes mainly influence the predicted sharp pressure peak.

The Sound Pressure Level (SPL) are calculated for the recorded pressure signal from the model scale simulation (the grey line in figure 3.25 but unscaled), as shown in Equation 3.2, and plotted in figure 3.27 with comparison to experimental measurements at the same location. The local SPL is rich in higher order BPFs, as the predicted pressure fluctuation contains very sharp peaks in each blade passages and resulted similarly in a signal with repeated unit impulses, which includes all frequencies.

$$L_p = 20log_{10}(\frac{p}{p_{ref}}), \quad p_{ref} = 1\mu Pa. \tag{3.2}$$

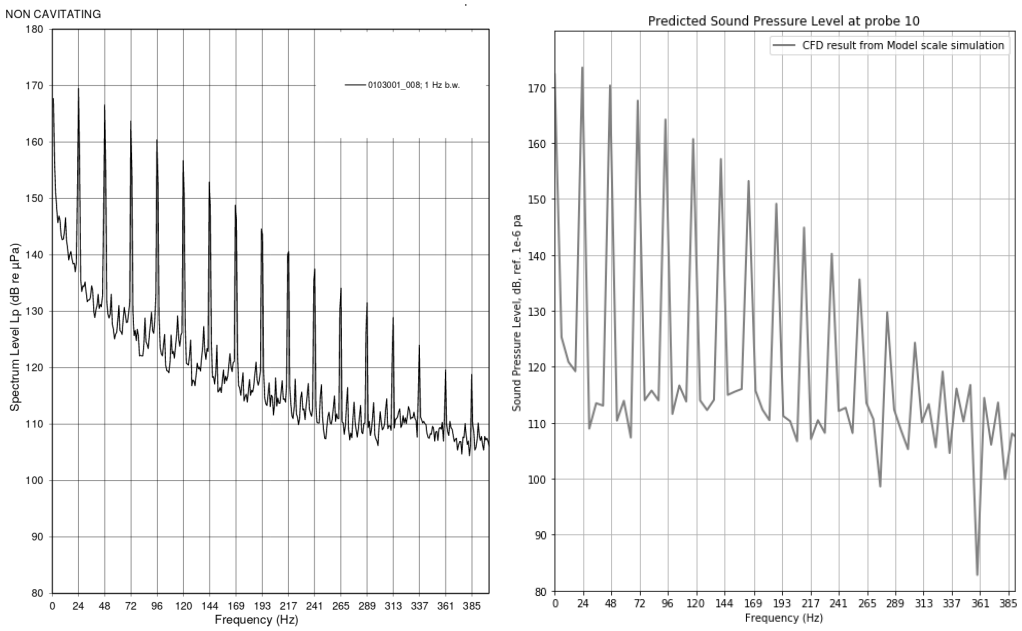

(a) Experimental measurement

(b) CFD model scale prediction

Figure 3.27: Comparison of sound pressure level at probe 10

The summary of pressure pulse levels for the cavitating conditions are shown in figure 3.28, while the cavitation patterns in the experiment and simulations are shown for blade phase of 22.5 degrees in figure 3.29. The cavitation number was calculated based on full-scale ship operating condition at 0.75 propeller diameter at the upper-most position with assumed wake height 0.75 m. Gravity was not considered in condition A and B, to make the conditions comparable.

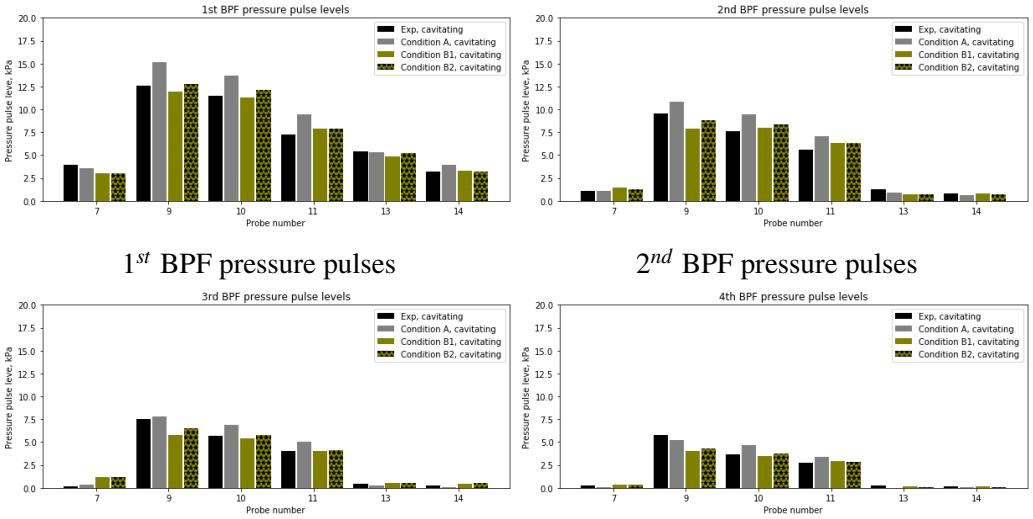

1^{st} BPF pressure pulses

2^{nd} BPF pressure pulses

3^{rd} BPF pressure pulses

4^{th} BPF pressure pulses

Figure 3.28: Pressure pulse levels on different probe points, cavitating condition

(a) Exp recording

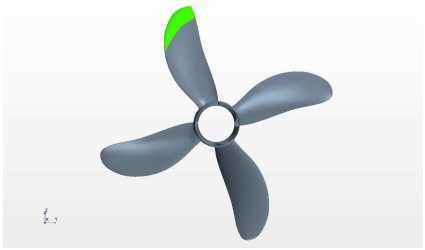

(b) Condition A

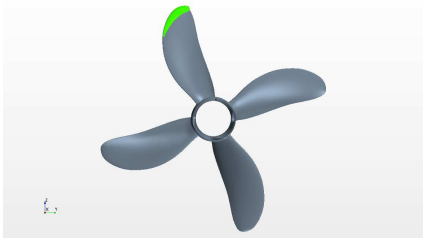

(c) Condition B1

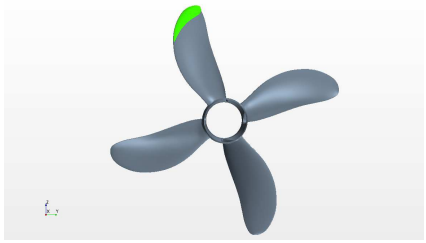

(d) Condition B2

Figure 3.29: Cavitation patterns at blade phase of 22.5 degrees

The predicted pressure fluctuation signals on probe number 10 is shown in figure 3.30. Compared to non-cavitating simulations, the pressure fluctuations increased after each spike, due to the dynamics of cavitation. However, these fluctuations are stronger in model scale than in full scale simulations. The predicted thrust coefficients and torque coefficients are summarized in figure 3.31. The influence of cavitation on propeller propulsion performance is small.

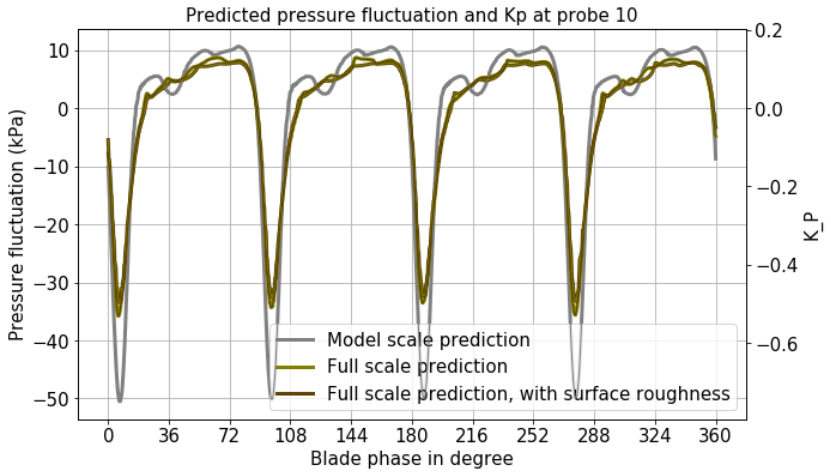

Figure 3.30: Predicted pressure fluctuations on probe 10, cavitating conditions

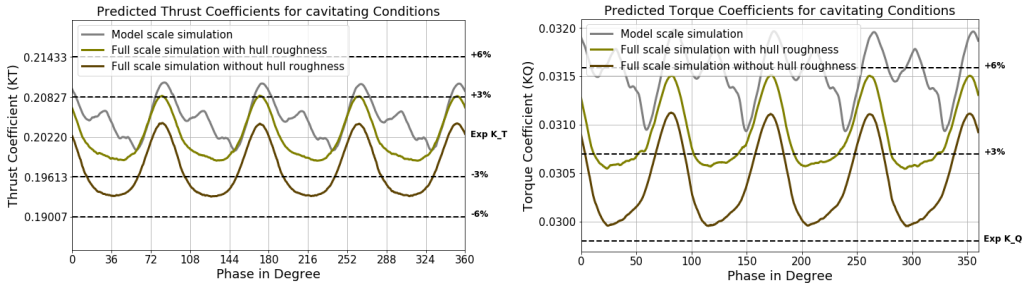

Figure 3.31: Predicted thrust and torque coefficients for non-cavitating conditions

The wave pattern predicted for condition C at the simulation time of 60s is shown in figure 3.32. Some disturbances are found outside the Kelvin wave region but the results are not expected to be influenced.

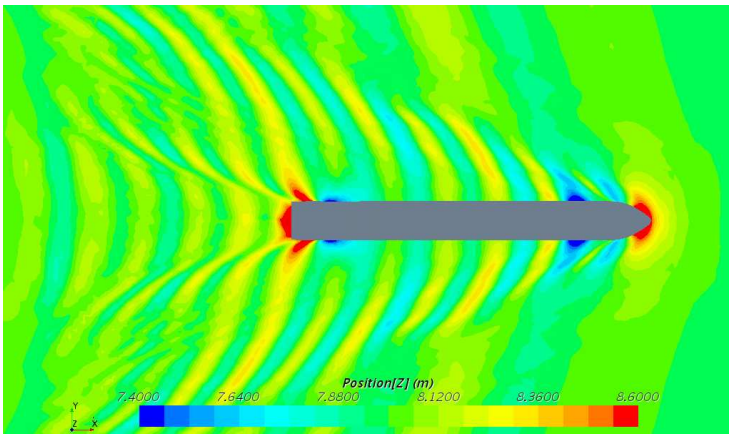

Figure 3.32: Predicted wave pattern

The predicted pressure pulse levels are summarized in figure 3.33. Same level of accuracy was also obtained for cavitating conditions as non-cavitating condi-

tions, except the 2^{nd} order BPF pressure pulses at probe point number 7, 11, 13 and 14. Generally the predicted results agree well with experimental data and the differences between non-cavitating and cavitating condition are relatively small, but at the mentioned probe locations the 2^{nd} order BPF pressure pulses are over-predicted, and the reason is not known. The pressure fluctuation history for probe number 7 and 10 are plotted in figure 3.34. Comparing the two pressure signals, similar variation in probe No. 7 as is observed in probe No. 10 is seen (both are located close to each other on the center line of the hull above the propeller), while the higher order harmonics are well predicted in probe No. 10.

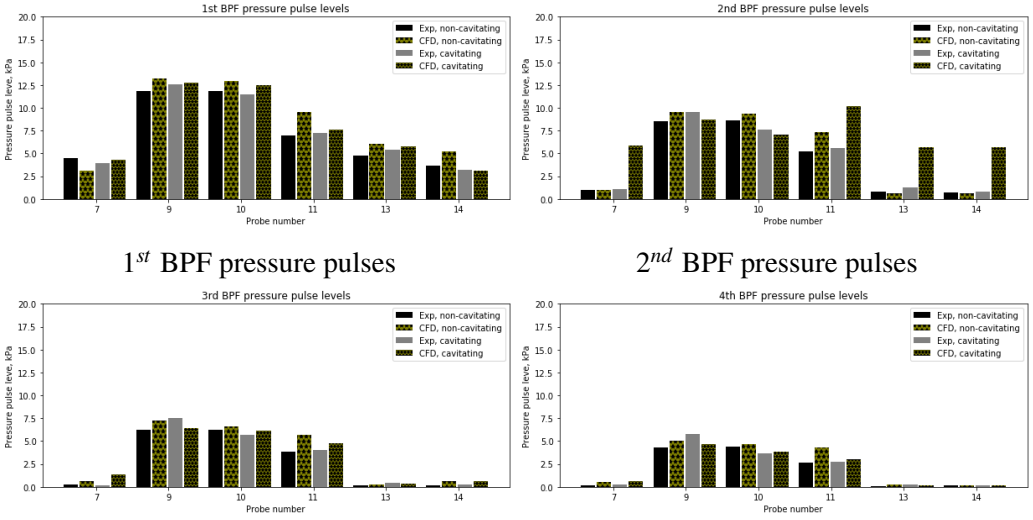

1^{st} BPF pressure pulses

2^{nd} BPF pressure pulses

3^{rd} BPF pressure pulses

4^{th} BPF pressure pulses

Figure 3.33: Pressure pulse levels on different probe points, condition C

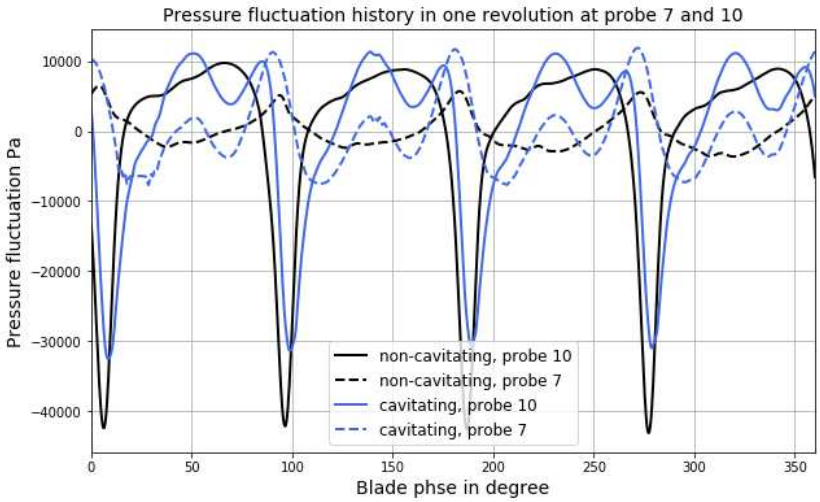

Figure 3.34: Predicted pressure fluctuations at probe 7 and probe 10

The predicted cavitation pattern at different blade positions are shown in figure 3.35. Cavity extent is slightly changed compared with the case B2, due to both the changed hydrostatic pressure - as the wave elevation is different and that for this case gravity is considered in the simulation - and the change in inflow conditions - as boundary condition is of different shape compared with the double body simulation of B2.

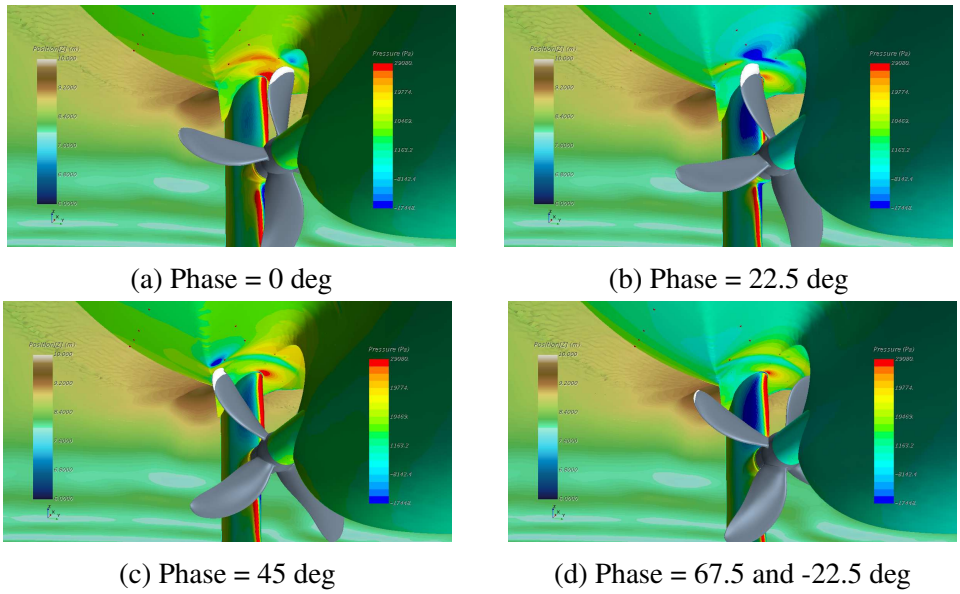

(a) Phase = 0 deg

(b) Phase = 22.5 deg

(c) Phase = 45 deg

(d) Phase = 67.5 and -22.5 deg

Figure 3.35: Cavitation patterns predicted in condition C

4

Summary and future work suggestions

Summary

In the present thesis, numerical predictions of propeller induced pressure pulses are presented and compared with available experimental measurements. The simulated conditions include model scale propeller mounted on inclined shaft, model scale propeller operating in behind-hull condition, and full scale propeller operating in behind hull condition with and without free surface.

The first question is about the maturity of prediction of the present RANS approach regarding 1^{st} blade passing frequency pressure pulses. Generally speaking the blade harmonic pressure pulses induced by a propeller in behind conditions is shown to be reasonably predicted by the present RANS approach for both non-cavitating and cavitating conditions. However, to maintain prediction accuracy, the accurate prediction of the ship wake is of vital importance. The difference could be up to 40% regarding 1^{st} order BPF pressure pulse between a well-resolved wake and a poorly resolved wake. The extent of sheet cavitation and its variation can also be reasonably predicted. For the two Kongsberg high-skew propellers operating under nearly uniform inflow conditions, numerical prediction is rather different from experimental measurements and the prediction could be misleading. Further studies reveals that the lack of sensitivity to laminar flow in the cavitation mass transfer model could be the major reason and modified models were used for improved cavitation prediction by using a transition sensitive turbulence model.

The second question is about the prediction ability regarding 2^{nd} order and higher orders BPF pressure pulse predictions. In the present study all the studied cases in behind conditions the predicted pressure pulses are rich in higher order BPFs including the 2^{nd} order BPF. The studied cases revealed different mechanisms inducing (numerical predicted) higher order BPF pressure pulses.

- For the general cargo vessel with LDP, the high order BPF pressure pulses result directly from the very small tip clearance. Signal analysis shows that

these high order components are not coming from tip vortex dynamics as is normally argued, but from the short pressure peaks when the blade is passing close to the hull. The short pressure peaks resulted similarly to a signal with repeated unit impulses and FFT analysis of a this signal will lead to high order components. Cavitation do not really excit higher values of pressure pulses in this case. One reason is that the pressure peaks come from the blade suction side while cavitation actually set lower limits of local pressure to saturation pressure. The other reason is that the propeller is rather lightly loaded, thus the cavitation volume is small and its variation is not large sweeping by the hull surface.

- For the container vessel, higher order BPF pressure pulses were predicted as well. The concluded reason is related to the sheet cavity closure, including interactions between side-entrant jet and tip vortex as well as interactions between sheet cavitation and ship wake. The starting of tip vortex bursting is clearly related with the side-entrant jet and sheet cavity collapse, and the tip vortex cavitation keeps rebounding outside the ship wake. The pressure pulses generated by tip vortex cavitation is up to 10^{th} BPF, as deduced by the isolated vapor volume in the tip region. The study also verified the fact that pulsing tip vortex cavitation is a monopole acoustic source. The predicted results using the base mesh also reveals the fact that without resolving tip vortex cavitation, higher order BPFs pressure pulses would also be predicted due to sheet cavity collapse.

Mesh spatial distribution is another topic here. In the present thesis the mesh studies were conducted considering three aspects:

- Mesh study was performed for the Kongsberg high-skew propellers with global refinement and the study revealed that for non-cavitating conditions a rather coarse mesh could provide reasonable enough predictions.

- Mesh influence of bare hull wake prediction was investigated for the container vessel case. For the case without free surface and appendages, 8 million cells seems to be a lower limit for boundary layer resolved mesh with corresponding region refinements. The lack of the number of prism layers may lead to an undesired transition ratio between last prism layer cell height and core mesh size and a diffusive wake might be predicted.

- Another mesh related investigation is the tip refinement regarding tip vortex cavitation predictions in the container vessel study. The base mesh and tip refined mesh were both used and compared. Much more tip vortex cavitation dynamics and higher order BPFs pressure pulses were predicted using the tip refined mesh.

Scaling between different scales or Reynolds number is also investigated in the present study. The major effective factor here is the wake influence regarding

blade load and sheet cavitation. For a higher Reynolds number scaled case, the pressure pulses are typically lower due to the thinner boundary layer and more compressed wake. This agree with observations in the literature though the influence of blade harmonic pressure pulse are generally smaller. Tip vortex and tip vortex cavitation, which are known to be another highly Reynolds number dependent phenomenon, are not included in the present study.

- In the study case of the general cargo vessel with LDP, simulations based on model scale configurations and simulations based on full scale configurations were performed and compared. The hull Reynolds number differs about 150 times between the two and higher values of extrapolated pressure pulses were predicted in model scale than in full scale. Tip vortex cavitation related phenomenon are not studied in the present case.

- In the study case of the container vessel, simulations based on model scale towing tank configurations and simulations based on model scale cavitation tunnel configurations were performed and compared in which hull Reynolds number differs about four times. Noticeable differences regarding sheet cavitation extent were found between the two conditions as well as blade frequency pressure pulse levels and small difference of tip vortex shape could also be found.

Future work suggestions

As shown in the container vessel case in the present study, the generation/collapse of tip vortex cavitation and the partial collapse of the sheet cavity, are the two major events generating high values of pressure pulses and contribute to the higher order BPFs. These two events are found to be highly dependent on the jet flows inside the sheet cavitation. Early in year 2001, as studied by Kuiper [53], this very common phenomena on ship propellers was discussed and the author pointed out that ”knowledge of sheet cavitation cannot remain restricted to its outer surface”. The jet flow has been widely studied on hydrofoils as re-entrant jet and for curved bodies it can be related to the convex shape of sheet cavity closure line. The present study shows that the ship wake may act as an important driving source regarding the formation of the jet flows. The formation of the jet flow, its interaction with ship wake, blade geometry and sheet cavitation can be further studied using more advanced approaches, which may provide fundamental knowledge of this common phenomena.

It can be of interest to use more advanced approaches to resolve the tip vortex cavitation in more details. The interaction with a more dynamic wake can be of interest as well. However, by using the present RANS approach, the tip vortex and tip vortex cavitation can be reasonably predicted within a short distance downstream the blade tip which covers the region of sheet cavitation and tip vortex cavitation interaction. Thus it may be more practical, as an engineering tool, to combine the RANS predicted tip flow information with empirical approaches

or theoretical tip vortex cavitation models, to include the contribution of tip vortex cavitation for broadband pressure pulses.

Further study regarding laminar and transitional flow and sheet cavitation inception is also of interest. The ships that have the needs to be assessed for pressure pulses and radiated noises, are usually designed with low values of pressure pulses and noise levels. For these cases the efficiency of propeller is less important and usually the sheet cavitation and tip vortex cavitation become the primary phenomena to be investigated. However, the over-predicted sheet cavitation in numerical simulations may change the development of vortical structures on the blade tip and prevent the formation of tip vortex cavitation. In order to match with experiments, this effect should be treated properly. The combination of transition sensitive turbulence model and mass transfer model seems to be an option but for investigation of mechanisms more advanced approach is preferred.

Lastly, there is still a gap between model scale predictions and full scale values. This is not only concerning the scaling effects of ship wake and pressure distribution on blades, but also concerning the differences regarding the mechanisms of cavitation developments. Performing full scale simulations directly can avoid some of the scaling effects, but as shown in the study in [54], the dynamics of model scale simulation agree well with experimental data including tip vortex cavitation dynamics, but the tip vortex cavitation was not captured in full scale simulations. This indicates that full scale simulations seems to be restricted in predicting tip vortex cavitation and high order BPF pressure pulses with moderate computational resources nowadays.

REFERENCES

[1] G. V. Frisk. Noiseonomics: The relationship between ambient noise levels in the sea and global economic trends. *Scientific reports*, 2:437, 2012.

[2] J. Tournadre. Anthropogenic pressure on the open ocean: The growth of ship traffic revealed by altimeter data analysis. *Geophysical Research Letters*, 41(22):7924–7932, 2014.

[3] R. M. Rolland, S. E. Parks, K. E. Hunt, M. Castellote, P. J. Corkeron, D. P. Nowacek, S. K. Wasser, and S. D. Kraus. Evidence that ship noise increases stress in right whales. *Proceedings of the Royal Society B: Biological Sciences*, 279(1737):2363–2368, 2012.

[4] E. McCarthy. *International regulation of underwater sound: establishing rules and standards to address ocean noise pollution*. Springer Science & Business Media, 2007.

[5] E. J. Foeth and J. Bosschers. Localization and source-strength estimation of propeller cavitation noise using hull-mounted pressure transducers. In *Proceedings of the 31st Symposium on Naval Hydrodynamics, Monterey, CA, USA*, pages 11–16, 2016.

[6] P. Pennings, J. Westerweel, and T. van Terwisga. Cavitation tunnel analysis of radiated sound from the resonance of a propeller tip vortex cavity. *International Journal of Multiphase Flow*, 83:1–11, 2016.

[7] L. Berghult. Propeller induced tip vortex noise as function of blade area and blade -tip loading. In *Proceedings of the international conference on propeller cavitation (NCT's 50)*, 2000.

[8] F. Pereira, F. Salvatore, F. Di Felice, and M. Soave. Experimental investigation of a cavitating propeller in non-uniform inflow. In *Proceedings of the 25th ONR Symposium on Naval Hydrodynamics, St. Johns, Canada*, 2004.

[9] B. Aktas, M. Atlar, P. Fitzsimmons, and W. Shi. An advanced joint time-frequency analysis procedure to study cavitation-induced noise by using standard series propeller data. *Ocean Engineering*, 170:329–350, 2018.

[10] J. Bosschers. Investigation of hull pressure fluctuations generated by cavitating vortices. In *First international symposium on marine propulsors SMP*, volume 9, 2009.

[11] B. Maines and Roger E. A. Arndt. The case of the singing vortex. *Journal of fluids engineering*, 119(2):271–276, 1997.

[12] P C. Pennings, J. Bosschers, J. Westerweel, and T J C. Van Terwisga. Dynamics of isolated vortex cavitation. *Journal of Fluid Mechanics*, 778:288–313, 2015.

[13] J. Bosschers. Analysis of inertial waves on inviscid cavitating vortices in relation to low-frequency radiated noise. In *WIMRC Cavitation Forum*. Warwick University UK, 2008.

[14] J. W. English. Cavitation induced hull surface pressures–measurements in a water tunnel. 1980.

[15] A. Konno, K. Wakabayashi, H. Yamaguchi, M. Maeda, N. Ishii, S. Soejima, and K. Kimura. On the mechanism of the bursting phenomena of propeller tip vortex cavitation. *Journal of marine science and technology*, 6(4):181–192, 2002.

[16] G. Bark and R. E. Bensow. Hydrodynamic mechanisms controlling cavitation erosion. *International Shipbuilding Progress*, 60(1-4):345–374, 2013.

[17] E. van Wijngaarden, J. Bosschers, and G. Kuiper. Aspects of the cavitating propeller tip vortex as a source of inboard noise and vibration. In *ASME 2005 Fluids Engineering Division Summer Meeting*, pages 539–544. American Society of Mechanical Engineers, 2005.

[18] R. E. Bensow and R. Gustafsson. Effect of propeller tip clearance on hull pressure pulses. In *Proceedings of the 5th International Symposium on Marine Propulsors*, 2017.

[19] K W. Shin and P. Andersen. Cfd analysis of propeller tip vortex cavitation in ship wake fields. In *Proceedings of the 10th International Symposium on Cavitation (CAV2018)*. ASME Press, 2018.

[20] F. Miglianti, F. Cipollini, L. Oneto, G. Tani, and M. Viviani. Model scale cavitation noise spectra prediction: Combining physical knowledge with data science. *Ocean Engineering*, 178:185–203, 2019.

[21] P. Perali, T. Lloyd, and G. Vaz. Comparison of urans and bem-bem for propeller pressure pulse prediction: E779a propeller in a cavitation tunnel. In *Proceedings of 19th Numerical Towing Tank Symposium, 3rd-4th October, St. Pierre dOléron, France*, 2016.

[22] K J. Paik, H G. Park, and J. Seo. Rans simulation of cavitation and hull pressure fluctuation for marine propeller operating behind-hull condition. *International Journal of Naval Architecture and Ocean Engineering*, 5(4):502–512, 2013.

[23] K. Fujiyama. Numerical simulation of ship hull pressure fluctuation induced by cavitation on propeller with capturing the tip vortex. In *Fourth International Symposium on Marine Propulsors*, 2015.

[24] D Q. Li, J. Hallander, and R. Karlsson. Progress in predicting pressure pulses and underwater radiated noise induced by propeller with pressure side cavitation. In *Numerical Towing Tank Symposium (NuTTS 2015), Cortona, Italy*, 2015.

[25] N. Sakamoto and H. Kamiirisa. Prediction of near field propeller cavitation noise by viscous cfd with semi-empirical approach and its validation in model and full scale. *Ocean Engineering*, 168:41–59, 2018.

[26] D Q. Li, J. Hallander, and T. Johansson. Predicting underwater radiated noise of a full scale ship with model testing and numerical methods. *Ocean Engineering*, 161:121–135, 2018.

[27] R. E. Bensow and M. Liefvendahl. An acoustic analogy and scale-resolving flow simulation methodology for the prediction of propeller radiated noise. In *31th Symposium on Naval Hydrodynamics, California*, 2016.

[28] R. E. Bensow and G. Bark. Implicit les predictions of the cavitating flow on a propeller. *Journal of fluids engineering*, 132(4):041302, 2010.

[29] A. Asnaghi. *Computational Modelling for cavitation and tip vortex flows*. PhD thesis, Chalmers University of Technology, 2018.

[30] A. Asnaghi, R. E. Bensow, and U. Svennberg. Comparative analysis of tip vortex flow using rans and les. 2017.

[31] C. T. Hsiao and G. L. Chahine. Scaling of tip vortex cavitation inception for a marine open propeller. In *27th Symposium on Naval Hydrodynamics, Seoul, Korea*, pages 5–10, 2008.

[32] B. Ji, X. Luo, X. Peng, Y. Wu, and H. Xu. Numerical analysis of cavitation evolution and excited pressure fluctuation around a propeller in non-uniform wake. *International Journal of Multiphase Flow*, 43:13–21, 2012.

[33] K. Shiraishi, Y. Sawada, D. Arakawa, and K. Hoshino. Experimental estimation for pressure fluctuation on ship stern induced by cavitating propeller using cavity shape measurements. In *Proceedings of the 10th International Symposium on Cavitation (CAV2018)*. ASME Press, 2018.

[34] T. Hoshino. Pressure fluctuation induced by a spherical bubble moving with varying radius. In *Transactions of the west-Japan society of naval architects 58*, pages 221–234. The Japan Society of Naval Architects and Ocean Engineers, 1979.

[35] G. Kuiper. Cavitation inception on ship propeller models. 1981.

[36] F. R. Menter. Two-equation eddy-viscosity turbulence models for engineering applications. *AIAA journal*, 32(8):1598–1605, 1994.

[37] P. A. Durbin. On the k-e stagnation point anomaly. *Int. J. Heat and Fluid Flow*, 17:89–90, 1996.

[38] F. Menter and T. Esch. Elements of industrial heat transfer predictions. In *16th Brazilian Congress of Mechanical Engineering (COBEM)*, volume 109, pages 117–127. sn, 2001.

[39] Florian R Menter, Martin Kuntz, and Robin Langtry. Ten years of industrial experience with the sst turbulence model. *Turbulence, heat and mass transfer*, 4(1):625–632, 2003.

[40] R. B. Langtry and F. R. Menter. Correlation-based transition modeling for unstructured parallelized computational fluid dynamics codes. *AIAA journal*, 47(12):2894–2906, 2009.

[41] R. B. Langtry. A correlation-based transition model using local variables for unstructured parallelized cfd codes. 2006.

[42] R. B. Langtry. Extending the gamma-rethetat correlation based transition model for crossflow effects. In *45th AIAA fluid dynamics conference*, page 2474, 2015.

[43] J. P. Franc and J. M. Michel. Attached cavitation and the boundary layer: experimental investigation and numerical treatment. *Journal of Fluid Mechanics*, 154:63–90, 1985.

[44] G. Wang, I. Senocak, W. Shyy, T. Ikohagi, and S. Cao. Dynamics of attached turbulent cavitating flows. *Progress in Aerospace sciences*, 37(6):551–581, 2001.

[45] M. V. Casey. The inception of attached cavitation from laminar separation bubbles on hydrofoils. In *Proc. of Conf. on Cavitation*, Edinburgh, 1974.

[46] Vijay H. Arakeri. Viscous effects on the position of cavitation separation from smooth bodies. *Journal of Fluid Mechanics*, 68(4):779–799, 1975.

[47] M. van Rijsbergen. A review of sheet cavitation inception mechanisms. 2016.

[48] Schiffbau-Versuchsanstalt Postdam. First international workshop on cavitation and propeller performance, 2011.

[49] Schiffbau-Versuchsanstalt Postdam. Second international workshop on cavitation and propeller performance, 2011.

[50] M. Rijsbergen and S. Beelen. A lagrangian analysis of scale effects on sheet cavitation inception. In *Sixth International Symposium on Marine Propulsors*, 2019.

[51] A. Reverberi, T. Lloyd, and G. Vaz. Towards cavitation modelling accounting for transition effects. 09 2016.

[52] G. H. Schnerr and J. Sauer. Physical and numerical modeling of unsteady cavitation dynamics. In *Fourth international conference on multiphase flow*, volume 1. ICMF New Orleans, 2001.

[53] G. Kuiper. New developments around sheet and tip vortex cavitation on ships propellers. *http://resolver. caltech. edu/cav2001: lecture. 007*, 2001.

[54] K. Fujiyama and Y. Nakashima. Numerical prediction of acoustic noise level induced by cavitation on ship propeller at behind-hull condition. In *Fifth International Symposium on Marine Propulsors (smp17), Espoo, Finland*, 2017.